

Siberian meimechites: origin and relation to flood basalts and kimberlites

A.V. Sobolev^{a,b,c,*}, S.V. Sobolev^{d,e}, D.V. Kuzmin^{b,f},
K.N. Malitch^g, A.G. Petrunin^{d,e}

^a Vernadsky Institute of Geochemistry and Analytical Chemistry, Russian Academy of Sciences, 19 ul. Kosygina, Moscow, 119991, Russia

^b Max Planck Institut für Chemie, 27 Joh.-Joachim-Becher-Weg, Mainz, 55128, Germany

^c Geowissenschaftliches Zentrum Göttingen, Abteilung Geochemie, Universität Göttingen, Goldschmidtstrasse 1, 37077, Göttingen, Germany

^d Deutsches GeoForschungsZentrum GFZ, Telegrafenberg, 14473, Potsdam, Germany

^e Schmidt Institute of the Physics of the Earth, Russian Academy of Sciences, 10 ul. B. Gruzinskaya, Moscow, 123995, Russia

^f Sobolev Institute of Geology and Mineralogy, Siberian Branch of the Russian Academy of Sciences,

3 prosp. Akad. Koptyuga, Novosibirsk, 630090, Russia

^g Karpinsky Russian Geological Research Institute (VSEGEI), Federal Agency of Mineral Resources, 74 Sredny Pr., St. Petersburg, 199106, Russia

Received 3 September 2009

Abstract

Here we combine petrological-geochemical and thermomechanical modeling techniques to explain origin of primary magmas of both Maimecha–Kotui meimechites and the Gudchikhinskaya basalts of Norilsk region, which represent, respectively, the end and the beginning of flood magmatism in the Siberian Trap Province.

We have analyzed the least altered samples of meimechites, their olivine phenocrysts, and melt inclusions in olivines, as well as samples of dunites and their olivines, from boreholes G-1 and G-3 within the Guli volcanoplutonic complex in the Maimecha–Kotui igneous province of the northern Siberian platform. The Mn/Fe and Ni/MgO ratios in olivines indicate a mantle peridotite source of meimechites. Meimechite parental magma that rose to shallow depths was rich in alkalis and highly magnesian (24 wt.% MgO), largely degassed, undersaturated by sulfide liquid and oxidized. At greater depths, it was, likely, high in CO₂ (6 wt.%) and H₂O (2 wt.%) and resulted from partial melting of initially highly depleted and later metasomatized harzburgite some 200 km below the surface. Trace-element abundances in primary meimechite magma suggest presence of garnet and K-clinopyroxene, in the mantle source and imply for genetic link to the sources of the early Siberian flood basalts (Gudchikhinskaya suite) and kimberlites. The analyzed dunite samples from the Guli complex have chemistry and mineralogy indicating their close relation to meimechites.

We have also computed thermomechanical model of interaction of a hot mantle plume with the shield lithosphere of variable thickness, using realistic temperature- and stress-dependent visco-elasto-plastic rocks rheology and advanced finite element solution technique.

Based on our experimental and modeling results we propose that a Permian–Triassic plume, with potential temperature of about 1650 °C transported a large amount of recycled ancient oceanic crust (up to 15%) as SiO₂-oversaturated carbonated eclogite. Low-degree partial melting of eclogite at depths of 250–300 km produced carbonate-silicate melt that metasomatized the lithospheric roots of the Siberian shield. Further rise of the plume under relatively attenuated lithosphere (Norilsk area) led to progressive melting of eclogite and formation of reaction pyroxenite, which then melted at depths of 130–180 km. Consequently, a large volume of melt (Gudchikhinskaya suite) penetrated into the lithosphere and caused its destabilization and delamination. Delaminated lithosphere that included fragments of locally metasomatized depleted harzburgite subsided into the plume and was heated to the temperatures of the plume interior with subsequent generation of meimechite magma. Meimechites showed up at the surface only under thicker part of the lithosphere aside from major melting zone above because otherwise they were mixed up in more voluminous flood basalts. We further suggest that meimechites, uncontaminated Siberian flood basalts and kimberlites all share the same source of strongly incompatible elements, the carbonated recycled oceanic crust carried up by hot mantle plume.

© 2009, IGM, Siberian Branch of the RAS. Published by Elsevier B.V. All rights reserved.

Keywords: olivine; meimechite; pyroxenite; eclogite; carbonatite; kimberlite; recycled crust; metasomatism; thermomechanical model; mantle plume; Siberian traps, Large Igneous Province

* Corresponding author.

E-mail address: alexander.sobolev@mpic.de (A.V. Sobolev)

Introduction

The Siberian Traps is the largest Phanerozoic flood basalt province of the Earth. Therefore, understanding of the physical and chemical processes that led to its formation is the first-order goal for geoscience. Multidisciplinary nature of those processes requires corresponding multidisciplinary analytical techniques. In the first part of this study we use geochemical and petrological methods while in the second part we employ results of the geochemical-petrological analyses to constrain thermomechanical model of the origin of the Siberian Trap Province focusing on the genesis of the meimechites.

Knowledge of the temperature and composition of primary magmas is the key point in understanding the origin of the Siberian Trap Province. The models of magmatism in the province that assume a peridotitic source with a relatively low temperature of ~1350 °C corresponding to convecting upper mantle (McKenzie and Bickle, 1988) require rapid and significant thinning of continental lithosphere to generate the respective large amounts of magma from peridotite (Elkins-Tanton and Hager, 2000). With a temperature above that of convecting mantle, e.g., in the case of a mantle plume (Campbell and Griffiths, 1992; Dobretsov, 2008; White and McKenzie, 1995), a large amount of magma may be generated at relatively large depths, especially from olivine-free fusible mantle sources (Cordery et al., 1997; Sobolev et al., 2007, 2009a; Tuff et al., 2005). Mantle temperatures can be inferred from the compositions of primary magmas and their mantle sources (Herzberg and O'Hara, 2002; Herzberg et al., 2007). For this meimechite, a highly magnesian ultramafic rock (Sheinman, 1947; Sobolev, 1976) with signatures of very low crustal contamination (Arndt et al., 1995; Carlson et al., 2006), is the best material in the Siberian province of flood basalts (Sobolev, 1936).

Meimechites of the Maimecha–Kotui igneous province mark the end (about 251 Ma) of trap magmatism in Siberia (Fedorenko and Czamanske, 1997; Kamo et al., 2003; Kogarko and Zartman, 2007; Vasiliev and Zolotukhin, 1995). They crystallized from Phanerozoic magma with the greatest MgO enrichment (over 25 wt.%) and, hence, the hottest temperature (Arndt et al., 1995; Sobolev and Slutsii, 1984; Sobolev et al., 1991). In this respect they match only Archean komatiites and thus provide one of few proofs for ultrahigh eruption temperatures (above 1550 °C) in Phanerozoic time. High crystallization temperatures of meimechites (above 1450 °C) were first predicted from homogenization of melt inclusions in olivine (Sobolev et al., 1972).

Abundant data on the major- and trace-element chemistry of meimechite primary magma, as well as on radiogenic Nd, Sr, and Os isotopes, indicate an origin with a significant contribution of deep (below 200 km) depleted mantle (Arndt et al., 1995; Carlson et al., 2006; Elkins-Tanton et al., 2007; Kogarko and Ryabchikov, 1995; Kogarko and Zartman, 2007; Ryabchikov et al., 2009; Sobolev et al., 1991). However, the role of volatiles and the relative percentages of peridotite and olivine-free components in the source remain unknown. Another poorly understood issue is the relation of meimechites

with older flood basalts and kimberlites in terms of chemistry and petrology of their mantle sources.

The objectives of this study have been (i) to infer the *PT* conditions of meimechite formation from their primary magma composition (including volatiles), (ii) to predict the phase composition of the mantle source, and (iii) to investigate the relation among meimechites, traps, and kimberlites. For this purpose we used new explicit analytical data on olivine phenocrysts and melt inclusions in them with reference to previous results (Kogarko and Ryabchikov, 2000; Ryabchikov et al., 2009; Sobolev and Slutsii, 1984; Sobolev et al., 1991) and to new models (Cartigny et al., 2008) and approaches (Sobolev et al., 2007). We especially consider the idea of involvement of the ancient subducted and recycled oceanic crust in the mantle magma generation processes (Allegre and Turcotte, 1986; Hofmann and White, 1982; Sobolev and Sobolev, 1975, 1977a, 1980). We suggest that the meimechite parental melt was rich in CO₂ (6 wt.%) and H₂O (2 wt.%) and originated at about 1600–1800 °C and 6–8 GPa within the mantle plume that gave rise to the Siberian Trap Province. Meimechites may have been derived from depleted peridotite which was metasomatized with carbonate-silicate melt resulting from low-degree partial melting of recycled oceanic crust. Meimechites may be related with associated traps and kimberlites as they had a common source of most incompatible elements coming from recycled oceanic crust entrained with a rising mantle plume.

Samples

Geological background and brief characteristics. The Maimecha–Kotui igneous province stretches over 70,000 km² on the northern end of the Siberian craton (Vasiliev and Zolotukhin, 1975, 1995). We sampled the area of the Guli volcanoplutonic complex controlled by the N-S Taimyr–Baikal and W-E Yenisei–Kotui paleorifts. According to processed gravity and drilling data, the complex has a form of a plate dipping to the northwest and looks like an ellipsoid in the map view, with its long axis extending in the NE direction (Malitch and Lopatin, 1997a).

In its exposed part, the complex consists mainly of ultramafic rocks of two phases: (i) dunites and chromitites and (ii) clinopyroxenites, with wehrlites and clinopyroxene-bearing dunites at the contact between the two phases. Dunites exist as a 30 km long and 10–15 km wide sickle-shaped body in the map view over an area of ~450 km² (Fig. 1). They lie under meimechites, ultramafic volcanics of the Maimecha suite, in the southwest, and in the center they are intruded by stocks of the Maimecha–Kotui ijolite-carbonatite complex occupying 30 km².

Meimechites of the Maimecha–Kotui province and the associated dunites and alkaline rocks of the Guli complex have bulk-rock Sm–Nd ages of 239 ± 61 Ma (Kogarko et al., 1988) and 231 ± 70 Ma (Kogarko et al., 1996), a bulk-rock U–Pb age of 250 ± 9 Ma (Kogarko and Zartman, 2007), and Ar–Ar biotite ages of 245.5 ± 1.2 and 243.8 ± 5.5 Ma (Dalrymple

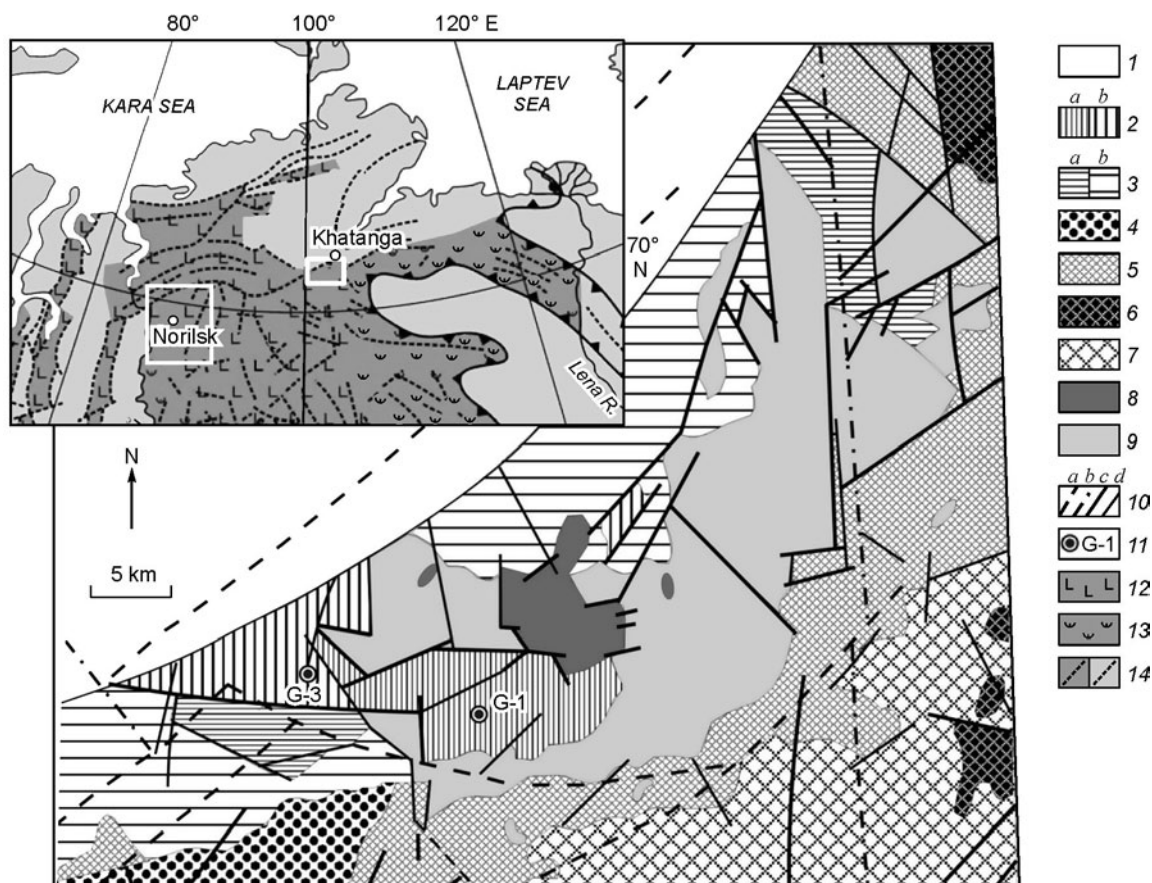


Fig. 1. Generalized geology of Guli complex, Maimecha–Kotui igneous province, northern Siberian craton, modified after (Malitch and Lopatin, 1997b; Malitch et al., 2002). Boxes in inset map are areas (Sobolev et al., 2009a) of most voluminous magmatism in Siberian craton around Norilsk and Khatanga (Maimecha–Kotui province). 1, terrigenous sediments (J₃–K₁) in Khatanga basin; 2, picrite-meimechite complex (T_{1–2}), meimechite and porphyry picrite: Maimecha suite (a), subvolcanic and dike facies (b); 3, Del'kan suite (T₁): trachybasalt and andesite (a), augite, limburgite, and nephelinite (b); 4, Tyvankit suite (T₁): trachybasalt and trachybasaltic andesite; 5, Kogotok suite (T₁): basalts; 6, Arydzhang suite (P₂–T₁): alkali picrite, phoidite, and alkali leucobasalt; 7, Pravoboyarka suite (P₂–T₁): mafic pyroclastic rocks; 8, ijolite-carbonatite complex (T₂): alkali-ultramafic and alkaline rocks and carbonatites; 9, clinopyroxenite-dunite complex (D₃–C₁): dunite, chromite, and clinopyroxenite; 10, faults: (a) Yenisei–Kotui system, (b) Sayan–Anabar system, (c) magma venting faults at craton base, (d) faults in sediments; 11, drilling sites. In inset: 12, 13, flood volcanics: lavas (12) and tuff (13); 14, magma venting faults; solid black line with black triangles outlines boundary of Siberian Traps Province.

et al., 1995). Furthermore, there are precise Pb–Pb zircon and perovskite ages, respectively, for the stratigraphically lower rocks of the Delkan (251.1 ± 0.3 Ma) and Arydzhang (251.7 ± 0.4 Ma) suites (Kamo et al., 2003). Thus, judging by their available precise U–Pb and Ar–Ar ages and stratigraphic position, meimechites were the last lavas of the major flood volcanic event (trap magmatism) in the Siberian craton (Kamo et al., 2003). At least a part of the Guli dunites lie on the same Sm–Nd and U–Pb isochrons as meimechites, and therefore must be of proximal ages (Kogarko et al., 1988, 1996; Kogarko and Zartman, 2007). However, some workers argue that dunites may be much older than meimechites (Malitch, 2004; Malitch and Lopatin, 1997a; Zhabin, 1965).

The samples we studied were taken from boreholes G-1 and G-3 (Fig. 1) drilled for 1:200 000 geological surveys within the Guli area (Malitch et al., 1997a,b).

Borehole G-1 is located in the left side of the Poiskoviy Brook, a left tributary of the Dunitovaya River, 3.3 km upstream of the river mouth. There are bedrock exposures of

meimechites 25 m northwest of the borehole, which have a visible thickness of 185 m and form several steps in the relief. The rocks have distinct porphyric textures with olivine phenocrysts from 1.5 mm to 1.5 cm in size, or, more rarely, olivine aggregates, often fractured. The G-1 section to a depth of 401 m consists of dominating meimechites and subalkaline picrite porphyry and smaller amounts of dunites or less often clinopyroxenites (possibly, as xenoliths), as well as thin melanephelinite and malignite dikes.

Borehole G-3 is located in the left side of the Maimecha River, 9.3 km (azimuth 97°) upstream of the mouth of the Del'kan River, a left tributary of the Maimecha. The 400 m deep section of G-3 strips subvolcanic facies of meimechites and subalkaline picrite porphyry mapped within a picrite-meimechite complex (Malitch and Lopatin, 1997a,b).

For analytical work, we selected the least altered representative samples of meimechite and dunite. The petrography of the Guli meimechites and dunites being largely reported in

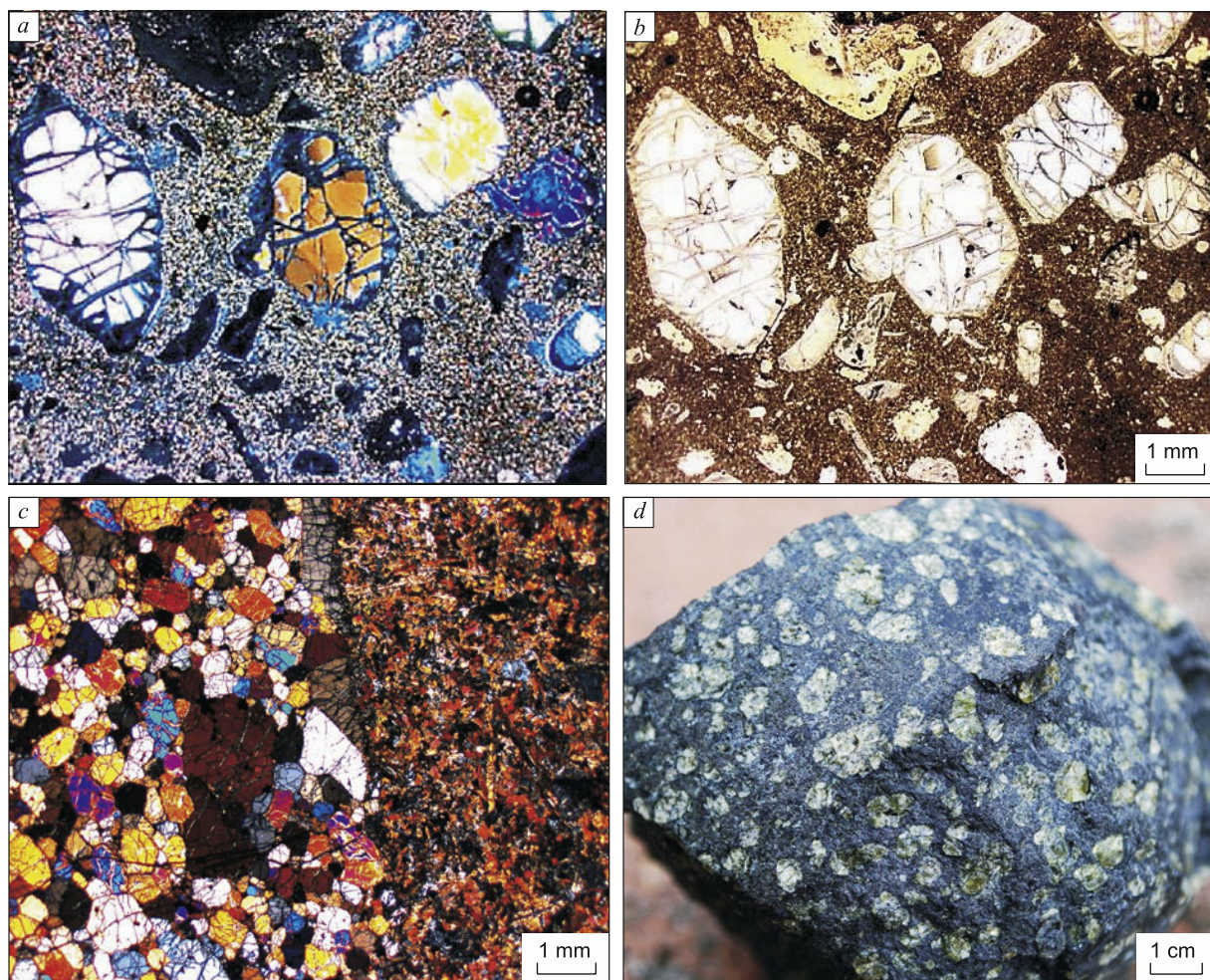


Fig. 2. Photographs of meimechite and dunite samples. *a, b*: thin section of meimechite, sample G-3 (2177), polarized and nonpolarized transmitted light; *c*: thin section of contact between dunite (left) and aphyric meimechite, sample G-1-22 (310.2), polarized light; *d*: sample of meimechite G-3 (2994).

the literature (e.g., Vasiliev and Zolotukhin, 1975), we confine ourselves to a brief outline.

The analyzed meimechites (samples G-1-25, core depth 301.3 m; G-1-32, 7.5 m; G-3 (2177), 217.7 m; G-3 (2994), 299.4 m) are porphyric rocks with 30–70% phenocrysts, mostly of well-faceted prismatic olivines reaching a size of 1 cm (Fig. 2, *a, b, d*) on the long axis, or much less often with clasts or aggregates of olivine crystals. Olivine phenocrysts contain inclusions of trapped crystallized melt or Cr-spinel. Cr-spinel also occurs as sporadic octahedral phenocrysts up to 1 mm. The meimechite matrix varies from vitreous to fully crystallized and consists of small olivines (commonly serpentinized), prismatic clinopyroxenes (Ti-augite), Ti-spinels, phlogopites, and altered glass.

Secondary alteration products are serpentine and magnetite, the former following cracks and rims of olivine phenocrysts and substituting for matrix olivine and glass.

The analyzed dunites (samples G-1-18, 312.3 m; G-1-22, 310.2 m) have euhedral inequigranular textures and consist of olivine (90–95%), including at serpentinized sites, up to 4% Cr-spinel, 1–6% phlogopite, and 1–6% clinopyroxene

(Fig. 2, *c*). Olivine is most often well faceted and ranges in size from fractions of microns to 10 mm; phlogopite and clinopyroxene occur in interstices between olivine crystals and veins together with Ti-spinel; serpentine and magnetite develop after olivine.

The contact between meimechites and dunites was stripped at depths of 308.8 m (sample G-1-24) and 310.2 m (sample G-1-22, Fig. 2, *c*). At 308.8 m meimechites were found to crosscut dunites as thin veins, i.e., the former apparently emplaced after the latter.

Methods

Samples preparation. The rocks were powdered and baked to glass using an Ir heater (Stoll et al., 2008). Olivine phenocrysts of 1–0.5 mm size fractions were selected, placed in epoxy, extracted, and polished. Melt inclusions were extracted and polished individually for each grain.

Analytical procedures. The compositions of minerals and melt inclusions were studied by X-ray electron-microprobe

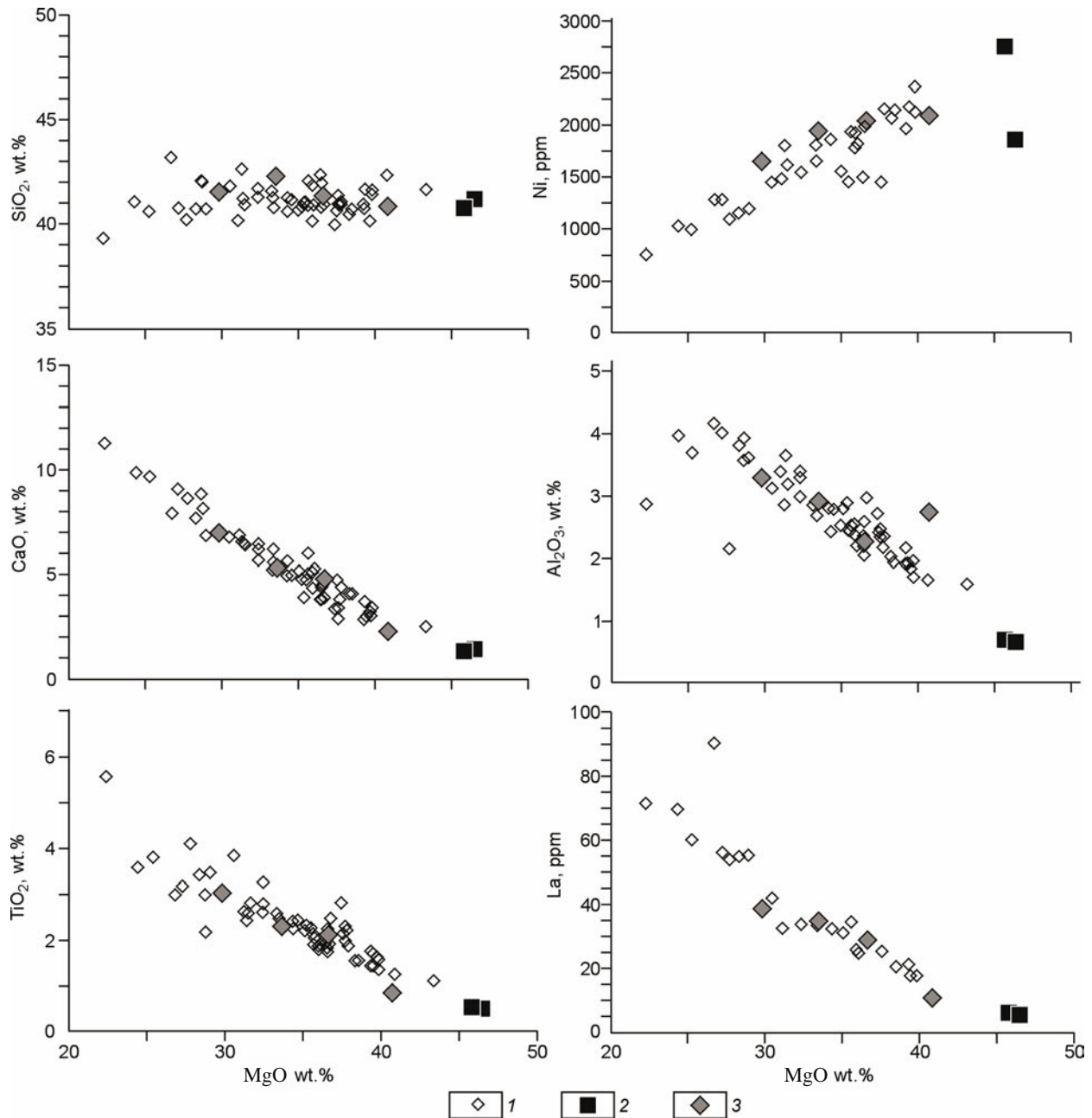


Fig. 3. Whole-rock compositions of meimechites and dunites. 1, compositions of meimechites borrowed from GEOROC database at <http://georoc.mpch-mainz.gwdg.de/georoc/>; 2, analyzed dunites; 3, analyzed meimechites.

analysis (EPMA), laser-ablation mass spectrometry with inductively coupled plasma (LA-ICP MS), and secondary-ion mass spectrometry (SIMS). Glasses were analyzed by EPMA and LA-ICP MS and powders by XRF on a *Philips MagiX Pro* spectrometer at Mainz University (Germany), Geological Department.

Major and trace elements were determined by EPMA on a *Jeol JXA 8200 SuperProbe* Electron Probe Microanalyzer at the Max Planck Institute for Chemistry (Mainz, Germany). Major-element abundances in glasses were measured at an accelerating voltage of 15 kV and a beam current of 12 nA with a reference sample of natural basaltic glass USNM111240/52 (VG2) (Jarosevich et al., 1980), with a

relative error of 1–2%. The compositions of olivines and some elements in inclusions were analyzed at an accelerating voltage of 20 kV and a beam current of 300 nA, following a special procedure which allows 20–30 ppm (two-sigma error) precision and accuracy for Ni, Ca, Mn, Al, Ti, Cr, and Co, and 0.02 mole percent for the forsterite component in olivine (Sobolev et al., 2007) and 20 ppm for Cl and S in glass.

LA-ICP MS was applied to determine trace elements in glasses of melt inclusions and in olivines, on an *ELEMENT-2*, *Thermo Scientific* mass spectrometer (GB) with a *UP-213 New Wave Research* solid-phase laser (GB) at the Max Planck Institute for Chemistry, with reference to the KL-2G and NIST 612 standard samples of basaltic glass (Jochum et al., 2000)

Table 1
Representative analyses of dunites and meimechites

Component	G-1-18 (312.3) dunite	G-1-22 (310.2) dunite	G-1-25 (301.3) meimechite	G-1-32 (7.5) meimechite	G-3 (2177) meimechite	G-3 (2994) meimechite
XRF						
SiO ₂ , wt.%	—	39.09	38.96	37.52	37.93	38.91
TiO ₂	—	0.46	2.87	0.76	2.00	2.14
Al ₂ O ₃	—	0.61	3.03	2.43	2.00	2.66
Fe ₂ O ₃	—	11.76	13.49	14.05	13.08	12.59
MnO	—	0.17	0.18	0.20	0.18	0.18
MgO	—	44.44	28.64	37.47	33.61	31.41
CaO	—	1.07	6.57	2.09	4.41	4.90
Na ₂ O	—	0.04	0.54	0.08	0.08	0.25
K ₂ O	—	0.15	1.08	0.19	0.42	0.43
P ₂ O ₅	—	0.04	0.35	0.08	0.24	0.26
Cr ₂ O ₃	—	0.587	0.239	0.436	0.386	0.245
NiO	—	0.318	0.195	0.256	0.234	0.235
LOI	—	1.94	4.52	5.48	6.47	6.68
Total	—	100.68	100.65	101.03	101.03	100.88
Sc, ppm	—	4	18	7	14	18
V	—	39	204	72	158	168
Cr	—	3581	1633	2591	2439	1716
Co	—	144	106	152	126	114
Ni	—	2465	1581	1991	1850	1802
Cu	—	28	109	36	74	84
Zn	—	74	81	86	90	94
Ga	—	3	11	11	6	10
Rb	—	5	24	8	12	16
Sr	—	72	458	130	230	322
Y	—	3	14	5	11	12
Zr	—	40	202	64	156	200
Nb	—	7	42	11	31	38
Ba	—	29	277	84	85	132
Pb	—	2	5	3	1	4
Th	—	0.2	2.2	1	1.5	1.4
U	—	0	1.3	0	1.5	2.6
EPMA (fused glass)						
SiO ₂ , wt.%	41.21	40.78	41.55	40.85	41.37	42.33
TiO ₂	0.49	0.52	3.02	0.84	2.15	2.31
Al ₂ O ₃	0.67	0.70	3.28	2.73	2.26	2.90
FeO	9.42	11.28	12.80	13.28	12.63	12.30
MnO	0.17	0.19	0.17	0.20	0.19	0.19
MgO	46.46	45.78	29.83	40.76	36.62	33.54
CaO	1.46	1.31	7.01	2.31	4.85	5.32
Na ₂ O	0.08	0.07	0.58	0.13	0.16	0.32
K ₂ O	0.15	0.15	1.08	0.18	0.44	0.42
P ₂ O ₅	0.03	0.05	0.35	0.09	0.28	0.29
S	0.00	0.01	0.00	0.00	0.00	0.00
Cl	0.00	0.00	0.00	0.00	0.00	0.00
Total	100.14	100.84	99.66	101.37	100.94	99.92
LA-ICP MS (fused glass)						
Rb, ppm	2.5	2.3	22.4	3.7	10.1	11.2
Ba	44.2	36.9	356	88.1	140	154
Th	0.65	0.69	3.53	1.01	2.78	3.40
U	0.17	0.18	0.92	0.23	0.60	0.78
Nb	7.96	7.51	45.5	11.9	34.5	37.6
Ta	0.49	0.44	2.85	0.77	2.17	2.40

Table 1 (continued)

Component	G-1-18 (312.3) dunite	G-1-22 (310.2) dunite	G-1-25 (301.3) meimechite	G-1-32 (7.5) meimechite	G-3 (2177) meimechite	G-3 (2994) meimechite
La	5.23	6.41	39.1	10.6	28.8	34.8
Ce	11.2	13.2	86.5	22.8	62.8	75.1
Pr	1.34	1.54	10.73	2.77	7.75	9.22
Nd	5.34	6.08	44.6	11.4	32.1	37.2
Sr	74.3	90.3	503	155	264	358
Sm	0.95	1.03	7.89	2.04	5.95	6.41
Zr	32.7	32.5	225	59.7	174	186
Hf	0.77	0.75	5.55	1.45	4.25	4.41
Eu	0.29	0.31	2.38	0.60	1.76	1.81
Ti	2974	3326	18254	4943	13180	13544
Gd	0.74	0.77	5.99	1.49	4.61	4.66
Tb	0.09	0.09	0.71	0.19	0.56	0.56
Dy	0.47	0.50	3.47	0.91	2.84	2.75
Ho	0.08	0.08	0.56	0.15	0.45	0.44
Y	1.97	1.96	13.33	3.57	10.92	10.73
Er	0.20	0.19	1.24	0.35	1.05	0.98
Tm	0.02	0.02	0.14	0.04	0.12	0.11
Yb	0.16	0.15	0.86	0.27	0.73	0.69
Lu	0.02	0.02	0.11	0.03	0.09	0.09
Ni	1858	2731	1651	2080	2028	1941
Cu	19.9	25.4	131	25.7	86.9	98.7
Mn	1191	1536	1472	1654	1519	1452
Sc	7.1	7.8	21.7	10.7	17.4	18.6
Zr	32.7	32.5	225	59.7	174	186
Co	125	165	113	151	135	120
Li	1.59	1.98	7.13	9.85	2.87	9.08
V	50.5	47.0	218.2	74.5	165	167

Note. XRF is X-ray Fluorescence analysis (Mainz University, Germany); EPMA is Electron-Probe Microanalysis (Max Planck Institute for Chemistry, Mainz, Germany); LA-ICP MS is laser-ablation mass spectrometry in inductively coupled plasma (Max Planck Institute for Chemistry, Mainz, Germany).

and the GeoRem database (<http://georem.mpch-mainz.gwdg.de>), and Ca as a reference element for glasses and Si for olivine. The typical laser diameter was 60–80 μm , and the ablation time was 60–80 s. The element abundances were determined with two-sigma errors of no more than 5 and 10% for concentrations above 1 ppm and ~ 0.1 ppm, respectively.

SIMS was used to measure H_2O contents in glasses of melt inclusions, on an *Ims3F*, *Cameca* ion microanalyzer (France) at the Max Planck Institute for Chemistry following the procedure reported in (Sobolev, 1996), with a relative error commonly within 10%. The detection limit for H_2O , estimated from ^1H of the host olivine was 0.02 wt.%.

Experimental procedure. Melt inclusions were studied on a specially designed low-inertia heating stage with optical control (Sobolev and Slutskii, 1984) in a pure He atmosphere, as in (Sobolev and Danyushevsky, 1994). The temperature was measured with a Pt₉₀Rh₁₀ thermocouple calibrated at the pure gold melting point in each run. The total exposure time at above 1000 °C was no more than 15 min, to avoid H_2O loss from inclusions.

In addition to the visual-control runs, we performed quench experiments in a vertical furnace with a controlled gas atmosphere, at the Vernadsky Institute of Geochemistry and

Analytical Chemistry (Moscow). The experiments were run in a H_2/CO_2 mixture at 1300 °C and an oxygen fugacity corresponding to the QFM buffer. The selected olivine crystals were placed into the furnace's hot zone in open Pt capsules.

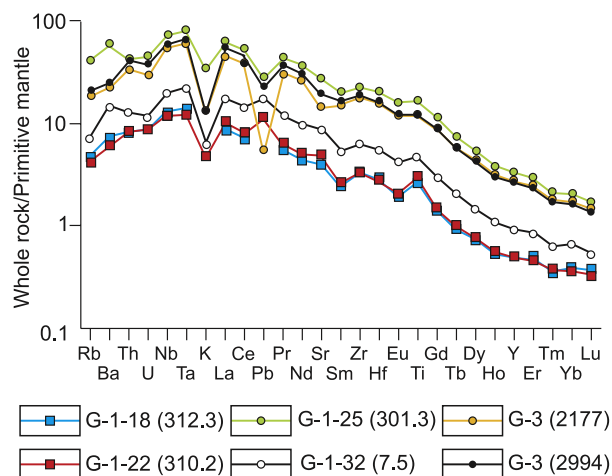


Fig. 4. Primitive mantle-normalized REE patterns of analyzed samples (Hofmann, 1988).

Table 2
Representative analyses of olivines from dunite and meimechite (wt.%)

Sample	Site	Fo	SiO ₂	TiO ₂	Al ₂ O ₃	FeO	MnO	MgO	CaO	NiO	CoO	Cr ₂ O ₃	Total	Mn/Fe	Ni*	X _{Pt} Mn	X _{Pt} Ni
G-3 (2994)	G-3a-8	91.93	40.73	0.039	0.062	7.85	0.129	50.14	0.313	0.414	0.016	0.114	99.80	0.0164	0.065	0.077	0.247
The same	G-3a-1	91.60	40.62	0.037	0.050	8.20	0.132	50.13	0.327	0.420	0.018	0.104	100.03	0.0161	0.069	0.145	0.287
The same	G-3a-50	91.43	40.59	0.034	0.044	8.31	0.131	49.78	0.294	0.425	0.016	0.094	99.72	0.0158	0.071	0.217	0.311
The same	G-3a-12	90.95	40.63	0.042	0.056	8.78	0.144	49.46	0.330	0.405	0.018	0.106	99.96	0.0164	0.072	0.082	0.321
The same	G-3a-23	90.74	40.51	0.038	0.055	8.97	0.144	49.31	0.330	0.400	0.019	0.101	99.88	0.0161	0.073	0.156	0.330
The same	G-3a-95	90.25	40.62	0.032	0.045	9.47	0.151	49.15	0.349	0.392	0.019	0.098	100.33	0.0159	0.076	0.178	0.359
The same	G-3a-81	89.77	40.43	0.035	0.042	9.90	0.168	48.68	0.408	0.379	0.019	0.077	100.13	0.0170	0.077	-0.036	0.375
The same	G-3a-33	89.31	40.33	0.039	0.046	10.31	0.167	48.32	0.418	0.369	0.021	0.071	100.08	0.0162	0.079	0.124	0.393
The same	G-3a-58	88.99	40.39	0.034	0.046	10.61	0.172	48.11	0.430	0.364	0.019	0.073	100.24	0.0162	0.080	0.122	0.409
The same	G-3a-96	88.81	40.26	0.037	0.043	10.76	0.176	47.90	0.407	0.358	0.021	0.065	100.02	0.0164	0.080	0.091	0.411
G-3 (2177)	G3-73	92.11	40.58	0.038	0.051	7.67	0.128	50.27	0.334	0.416	0.016	0.099	99.61	0.0167	0.063	0.025	0.232
The same	G3-34	91.85	40.65	0.039	0.060	7.94	0.131	50.14	0.353	0.402	0.015	0.108	99.83	0.0165	0.064	0.061	0.234
The same	G3-40	91.43	40.75	0.036	0.056	8.34	0.136	49.93	0.374	0.389	0.017	0.106	100.13	0.0163	0.065	0.104	0.248
The same	G3-3	91.07	40.75	0.041	0.057	8.68	0.145	49.63	0.390	0.372	0.017	0.098	100.18	0.0167	0.065	0.020	0.249
The same	G3-63	90.49	40.40	0.029	0.051	9.20	0.153	49.10	0.400	0.370	0.018	0.097	99.82	0.0166	0.069	0.035	0.294
The same	G3-7	90.12	40.61	0.029	0.042	9.57	0.158	48.94	0.389	0.350	0.021	0.092	100.20	0.0165	0.068	0.061	0.285
The same	G3-8	89.65	40.48	0.038	0.044	9.98	0.164	48.47	0.423	0.341	0.020	0.090	100.05	0.0164	0.070	0.076	0.303
The same	G3-50	89.27	40.36	0.038	0.051	10.34	0.173	48.23	0.429	0.349	0.019	0.084	100.06	0.0167	0.075	0.014	0.352
The same	G3-6	88.50	40.23	0.045	0.042	11.07	0.181	47.79	0.472	0.337	0.024	0.077	100.26	0.0164	0.078	0.093	0.386
The same	G3-2	87.11	40.06	0.043	0.041	12.31	0.202	46.68	0.554	0.324	0.021	0.055	100.29	0.0164	0.085	0.082	0.464
G-1-18 (312.3)	G1-18-72	89.69	40.01	0.042	0.028	9.88	0.169	48.18	0.515	0.306	0.019	0.037	99.18	0.0171	0.063	-0.064	0.224
The same	G1-18-23	89.61	40.18	0.045	0.031	9.98	0.170	48.27	0.507	0.306	0.019	0.036	99.55	0.0170	0.063	-0.048	0.230
The same	G1-18-29	89.60	40.20	0.055	0.028	9.98	0.173	48.24	0.454	0.303	0.019	0.027	99.47	0.0173	0.063	-0.111	0.224
The same	G1-18-60	89.58	40.24	0.043	0.026	10.02	0.171	48.31	0.512	0.302	0.020	0.030	99.68	0.0171	0.063	-0.056	0.223
The same	G1-18-25	89.56	40.24	0.043	0.031	10.03	0.170	48.26	0.468	0.298	0.020	0.029	99.58	0.0170	0.062	-0.032	0.216
The same	G1-18-1	89.54	40.25	0.059	0.015	10.08	0.172	48.42	0.565	0.301	0.021	0.020	99.90	0.0171	0.063	-0.054	0.224
The same	G1-18-63	89.53	40.26	0.058	0.014	10.06	0.171	48.25	0.514	0.299	0.019	0.019	99.66	0.0170	0.062	-0.041	0.220
The same	G1-18-24	89.51	40.18	0.044	0.044	10.08	0.173	48.24	0.539	0.305	0.019	0.040	99.67	0.0172	0.064	-0.076	0.235
The same	G1-18-15	89.48	40.18	0.038	0.028	10.14	0.171	48.37	0.531	0.306	0.019	0.034	99.82	0.0169	0.064	-0.012	0.239
The same	G1-18-31	89.44	40.09	0.040	0.019	10.17	0.177	48.31	0.411	0.305	0.019	0.021	99.55	0.0174	0.064	-0.126	0.240
G-1-32 (7.5)	G1-32-6	92.63	40.72	0.031	0.052	7.15	0.130	50.41	0.382	0.382	0.016	0.103	99.37	0.0182	0.054	-0.284	0.135
The same	G1-32-13	91.89	40.40	0.029	0.038	7.83	0.138	49.75	0.414	0.377	0.015	0.076	99.07	0.0176	0.059	-0.171	0.189
The same	G1-32-72	91.05	40.24	0.031	0.043	8.62	0.160	49.17	0.477	0.354	0.018	0.080	99.20	0.0186	0.062	-0.363	0.218
The same	G1-32-3	89.70	40.22	0.047	0.042	9.88	0.168	48.27	0.491	0.367	0.019	0.067	99.58	0.0170	0.075	-0.042	0.355

Table 2 (continued)

Sample	Site	Fo	SiO ₂	TiO ₂	Al ₂ O ₃	FeO	MnO	MgO	CaO	NiO	CoO	Cr ₂ O ₃	Total	Mn/Fe	Ni*	X _{Px} Mn	X _{Px} Ni
G-1-32 (7.5)	G1-32-68	88.92	40.12	0.042	0.046	10.60	0.179	47.72	0.447	0.350	0.019	0.073	99.59	0.0169	0.078	-0.016	0.383
The same	G1-32-17	88.05	39.88	0.042	0.051	11.38	0.191	47.04	0.466	0.347	0.021	0.093	99.50	0.0168	0.084	0.004	0.448
The same	G1-32-78	87.22	39.76	0.041	0.036	12.17	0.198	46.58	0.477	0.334	0.021	0.050	99.66	0.0163	0.087	0.111	0.483
The same	G1-32-89	86.97	39.77	0.035	0.036	12.36	0.206	46.26	0.527	0.327	0.023	0.047	99.58	0.0167	0.087	0.028	0.484
The same	G1-32-96	86.30	39.68	0.038	0.033	12.99	0.223	45.89	0.604	0.315	0.022	0.039	99.83	0.0172	0.089	-0.076	0.503
The same	G1-32-11	84.17	39.35	0.029	0.020	14.88	0.246	44.37	0.624	0.266	0.025	0.024	99.82	0.0165	0.089	0.055	0.503
G-1-25 (301.3)	G1-25-25	92.38	40.54	0.037	0.056	7.39	0.127	50.26	0.358	0.401	0.015	0.102	99.29	0.0172	0.059	-0.080	0.184
The same	G1-25-26	92.28	40.74	0.042	0.062	7.50	0.129	50.28	0.343	0.407	0.016	0.106	99.63	0.0172	0.061	-0.084	0.203
The same	G1-25-24	92.16	40.73	0.036	0.060	7.61	0.128	50.18	0.359	0.401	0.017	0.110	99.62	0.0168	0.061	-0.004	0.204
The same	G1-25-18	92.08	40.69	0.035	0.052	7.70	0.132	50.20	0.367	0.397	0.017	0.102	99.69	0.0171	0.061	-0.069	0.205
The same	G1-25-31	91.98	40.63	0.039	0.057	7.78	0.131	50.02	0.363	0.391	0.015	0.103	99.52	0.0168	0.061	-0.009	0.204
The same	G1-25-39	91.93	40.69	0.039	0.061	7.84	0.135	50.05	0.376	0.389	0.016	0.102	99.70	0.0172	0.061	-0.087	0.205
The same	G1-25-33	91.90	40.72	0.031	0.069	7.85	0.132	49.96	0.386	0.387	0.016	0.091	99.64	0.0168	0.061	-0.002	0.204
The same	G1-25-19	91.85	40.59	0.033	0.062	7.91	0.136	49.99	0.409	0.387	0.017	0.087	99.63	0.0172	0.061	-0.079	0.209
The same	G1-25-46	91.75	40.69	0.026	0.042	8.00	0.137	49.92	0.414	0.387	0.017	0.074	99.70	0.0171	0.062	-0.066	0.217
The same	G1-25-41	91.43	40.54	0.033	0.062	8.30	0.144	49.65	0.464	0.378	0.018	0.069	99.65	0.0174	0.063	-0.113	0.229
G-1-22 (310.2)	G1-22-1 cl	89.60	40.52	0.039	0.024	10.07	0.165	48.67	0.476	0.339	0.020	0.036	100.35	0.0164	0.070	0.082	0.302
The same	G1-22-1 rl	89.35	40.39	0.055	0.017	10.30	0.174	48.44	0.388	0.342	0.017	0.019	100.13	0.0169	0.073	-0.021	0.329
The same	G1-22-3 cl	89.24	40.20	0.054	0.017	10.38	0.177	48.29	0.539	0.341	0.018	0.025	100.03	0.0171	0.073	-0.053	0.336
The same	G1-22-3 rl	89.29	40.13	0.050	0.017	10.31	0.175	48.22	0.376	0.339	0.020	0.021	99.66	0.0170	0.073	-0.035	0.328
The same	G1-22-5 cl	89.61	40.46	0.038	0.029	10.05	0.168	48.64	0.464	0.347	0.021	0.043	100.26	0.0167	0.072	0.016	0.319
The same	G1-22-5 rl	89.29	40.52	0.029	0.012	10.37	0.175	48.49	0.404	0.341	0.019	0.022	100.39	0.0169	0.073	-0.015	0.332
The same	G1-22-6 cl	89.20	40.29	0.049	0.032	10.42	0.175	48.30	0.510	0.342	0.022	0.036	100.17	0.0168	0.074	0.001	0.340
The same	G1-22-6 rl	89.32	40.28	0.032	0.011	10.32	0.177	48.38	0.370	0.338	0.019	0.014	99.94	0.0172	0.072	-0.074	0.322
The same	G1-22-4 s	89.45	40.50	0.052	0.020	10.22	0.175	48.59	0.385	0.332	0.020	0.014	100.30	0.0171	0.070	-0.067	0.300
The same	G1-22-10 s	89.12	40.24	0.053	0.016	10.52	0.178	48.32	0.315	0.335	0.019	0.013	100.02	0.0169	0.073	-0.024	0.333
The same	G1-22-13 s	89.25	40.44	0.048	0.016	10.39	0.177	48.39	0.321	0.336	0.019	0.014	100.15	0.0170	0.072	-0.047	0.323
USNM 111312/444	AVG (21)	90.25	40.80	0.004	0.026	9.51	0.141	49.38	0.093	0.364	0.018	0.015	100.35	—	—	—	—
	SD	0.022	0.097	0.001	0.003	0.020	0.001	0.087	0.001	0.002	0.001	0.001	—	—	—	—	—
	RSD	0.02	0.24	39.17	11.15	0.21	0.60	0.18	1.32	0.63	5.82	8.56	—	—	—	—	—

Note. USNM 111312/444 is San-Carlos olivine, EMP standard of Smithsonian Institution (Jarosewich et al., 1980); AVG (21) is average bulk composition of San-Carlos olivine obtained for given measurement run, from 21 points; SD and RSD are standard deviation and relative standard deviation (%), respectively, for San-Carlos olivine; Ni* = NiO/(FeO/MgO); X_{Px}Mn and X_{Px}Ni are melt fractions of pyroxenite source in primary magma calculated from Ni and Mn in olivines (see text). cl is core of large crystals ($d > 500 \mu\text{m}$); rl is rim of large crystals; s is core of small crystals ($d < 100 \mu\text{m}$).

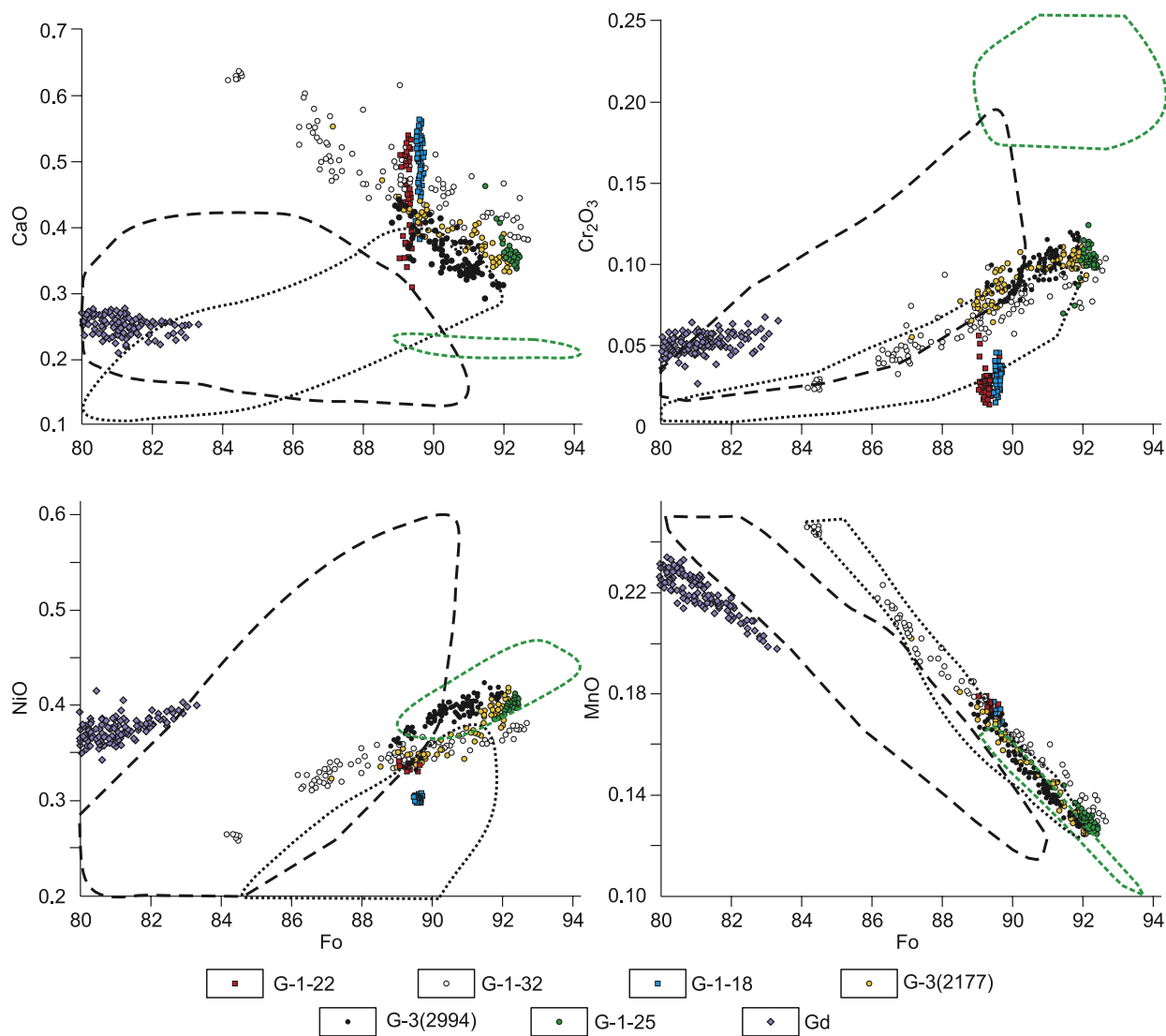


Fig. 5. Compositions of olivines in meimechites and dunites (wt.%). Gd, phenocrysts in olivine from picrites of Gudchikhinskaya suite, Norilsk area, after (Sobolev et al., 2009a). Fields contour olivine compositions as reported in (Sobolev et al., 2007), from MORB (dotted line), WPB on thick lithosphere of more than 70 km (dashed line), and peridotite komatiites (green dashed line).

After 15-min heating, the inclusions were quenched by automatic ejection of the Pt capsules into the cold zone.

For analysis we selected inclusions with sizes no smaller than 30 μm . The inclusions that partly or fully opened before or during the experiment were rejected according to measured Cl and S contents in glass (less than 0.02 wt.% Cl or S).

Numerical modeling. Fractional crystallization of meimechite melts was simulated with reference to the olivine-liquid equilibrium models of Ford et al. (1983) and Herzberg and O'Hara (2002) using the PETROLOG software (Danyushevsky, 2001). Correction for Fe-Mg exchange between melt inclusions and the olivine host was applied using the same models (Ford et al., 1983; Herzberg and O'Hara, 2002) with the software as in (Danyushevsky et al., 2000). The methods of thermomechanical modeling are specifically described in the corresponding section.

Compositions of rocks

The studied rock samples contain high MgO, which is consistent with a large amount of olivine phenocrysts. The abundances of all elements incompatible in olivine are inversely proportional to MgO (Fig. 3, Table 1) and follow the accumulation trend of magnesian olivine. All olivine-incompatible elements, except Ba, Rb, K, Na and Pb, correlate with MgO at more than 0.90 (R^2). The correlation of Ba, Rb, K, Na, and Pb with MgO is lower ($R^2 = 0.7\text{--}0.8$), possibly, because of alteration in secondary processes. The greatest MgO enrichment and depletion in incompatible elements are observed in dunites.

As it was noted in many publications, meimechites have high concentrations of lithophile elements coexisting with high MgO and Ni and low SiO₂ (Arndt et al., 1995; Kogarko and Ryabchikov, 1995; Sobolev and Slutski, 1984; Sobolev et al., 1991; Vasiliev and Zolotukhin, 1995). Another known feature

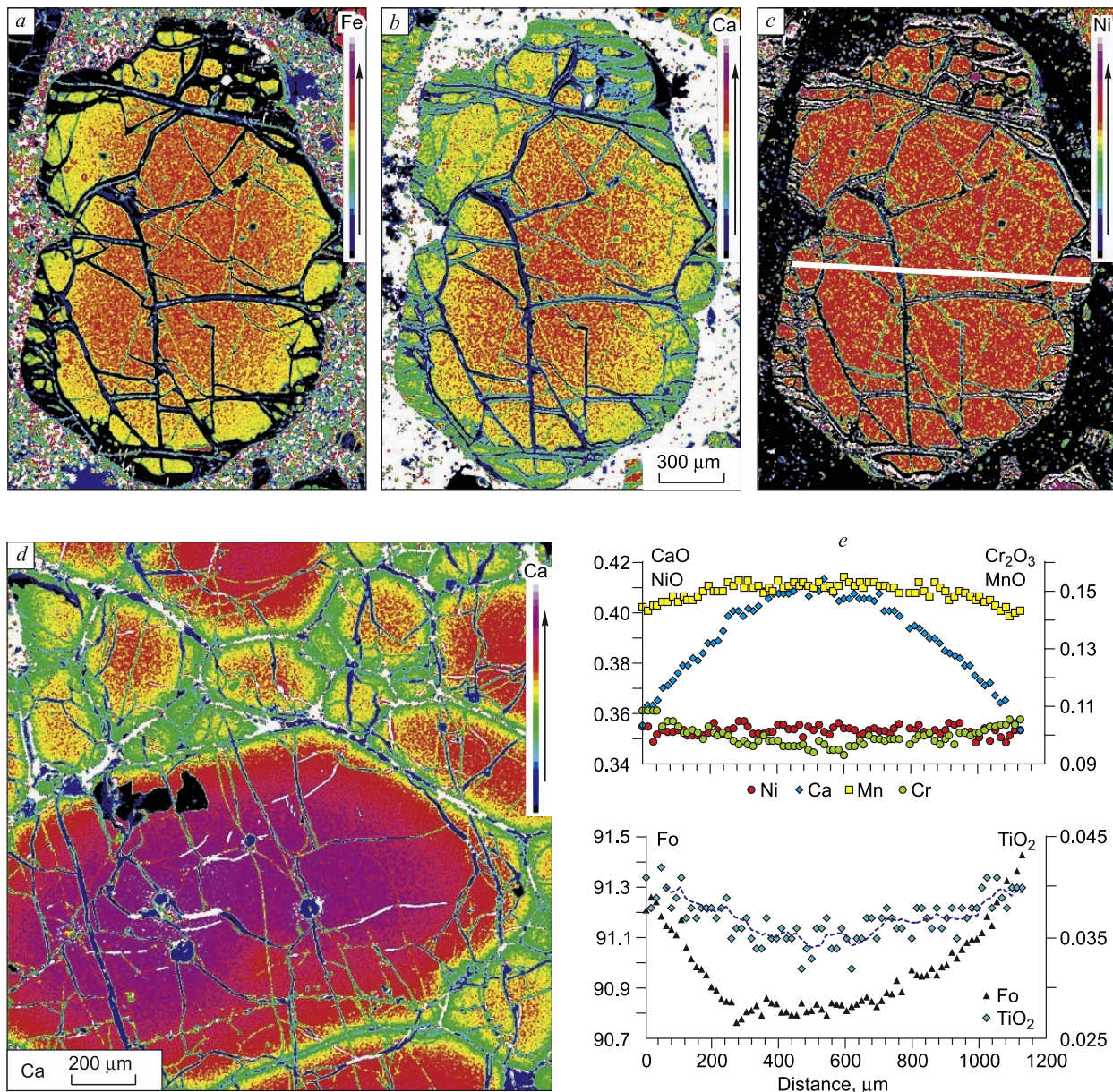


Fig. 6. Elemental maps (a–d) and profiles (e) of olivines from meimechite and dunite. a, b, c, olivine phenocryst from meimechite G-3 (2177); d, olivine phenocryst from dunite G-1-22; e, olivine phenocryst (a, b, c) from meimechite (profile position is shown by white line in c).

of meimechites (Arndt et al., 1995) is their marked depletion in typically garnet elements, such as HREE, Y, Sc, and Al (Fig. 4, Table 1). Furthermore, meimechites are relatively low in U and Th. Dunites show the same element patterns as meimechites but at lower concentration levels. The abundances of mobile elements involved in postmagmatic processes (Ba, Rb, K, Na and Pb) vary considerably and cannot be used a priori for estimating primary element abundances in magmas.

Composition of olivines

The composition of olivine phenocrysts in meimechites was reported in a number of earlier publications (Arndt et al., 1995;

Sobolev and Slutski, 1984; Sobolev et al., 1991; Ryabchikov et al., 2009; Vasiliev, 1978; Vasiliev and Zolotukhin, 1975). However, the new analyses presented in this study are more precise being obtained using a special procedure, with their quality checked with reference to the USNM 111312/444 standard of San-Carlos olivine (Table 2). Table 2 lists 62 representative compositions out of 565 recent analyses of olivines from meimechites and dunites. In order to compare data of proximal quality, we hereafter discuss only newly obtained compositions of olivines from meimechite and other mantle magmas and rocks (Sobolev, et al., 2007, 2009a; Sobolev, et al., 2008b, 2009b).

Olivine phenocrysts in meimechites (Figs. 5, 6 and Table 2) stand out in their high and variable MgO contents (Fo = 93–86) and high Ca, Mn, and Ti. Olivines are most often

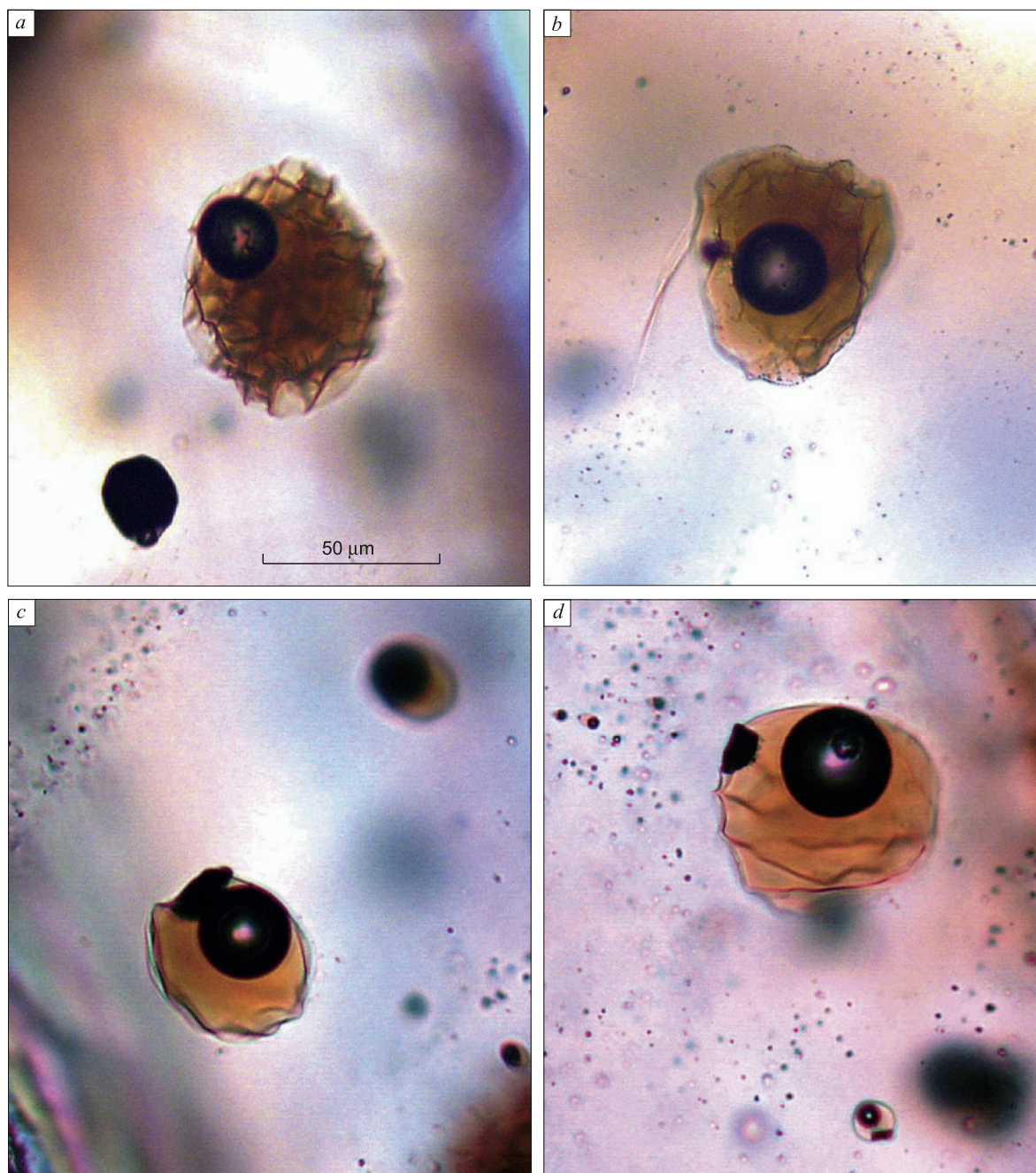


Fig. 7. Microphotographs of melt inclusions in olivine from meimechites quenched at 1300 °C. Brown transparent phase is silicic glass, round phase is gas (shrinkage bubble), dark solid phase is spinel.

unzoned, or occasionally have weak reverse zonation (Fig. 6, *a, b, c, e*) with MgO slightly increasing in wide rims together with decreasing Fe, Ca, Cr, Mn, increasing Ti and invariable Ni. Weak normal olivine zoning has been also reported by (Elkins-Tanton et al, 2007; Ryabchikov et al, 2009). Minor elements in olivines of the same Mg# may vary considerably (much above the error) within a sample. Note that olivine phenocrysts in different meimechite samples may differ strongly from one another.

Olivines from dunites (samples G-1-18, G-1-22) are similar to those from meimechites in Mg# and in Ti, Ca, and Mn contents, but the Fo component and Mn and Ni in the former

are less variable within a sample, though Ca and Cr vary notably. The latter variations correlate with grain sizes and with the distance from the outer rim (Fig. 6, *d*): Ca and Cr enrichment is the greatest in the cores of largest grains and the lowest in the rims and in the smallest grains. The contents of Fe, Mg, Ni, and Mn are uniform over the dunite olivines, and the crystals less than 50 μm and the rims (30–40 μm) are uniform with respect to all elements.

Olivines in meimechites have higher Mg# than in most of within-plate magmas (WPM) and MORB approaching Mg# of the most magnesian olivine in Archean peridotite komatiites (Fig. 3). The concentrations of MnO, and especially

Table 3
Representative analyses of melt inclusions in olivines from meimechites

Component	G-1-32*		G-1-32		G-1-32		G-1-32		G-1-32		G-1-32		G-1-32		G-3 (2994)		G-3 (2994)		G-1-25		
	70**	80	120	70	80	80	80	80	90	70	70	70	70	70	70	70	70	70	30	150	
Major elements in melt inclusions, wt. %																					
SiO ₂	43.98	43.41	42.46	42.85	42.64	41.95	41.39	41.18	42.60	40.78	42.16	41.82	41.10	42.38	41.61						
TiO ₂	5.69	4.28	5.85	5.34	6.22	4.90	6.14	5.29	5.91	6.33	5.53	5.67	5.97	5.53	4.69						
Al ₂ O ₃	7.64	7.67	7.07	7.79	7.38	6.29	7.45	6.34	6.36	7.30	7.82	7.31	7.47	7.26	6.30						
FeO	11.06	11.12	12.54	12.55	12.75	14.78	12.53	12.25	13.19	15.04	13.69	13.84	12.42	10.08	11.30						
MnO	0.16	0.15	0.18	0.18	0.18	0.19	0.16	0.18	0.18	0.18	0.17	0.18	0.15	0.14	0.14						
MgO	10.63	12.81	11.55	11.47	10.56	11.21	10.29	14.34	12.12	8.66	9.49	10.13	8.72	8.94	14.77						
CaO	12.66	13.62	12.96	13.16	12.22	13.10	13.94	12.63	15.57	15.26	13.57	14.54	15.51	15.94	12.54						
Na ₂ O	3.26	2.93	2.85	2.97	3.31	3.05	3.21	2.95	2.05	3.19	3.12	3.03	2.85	2.95	2.54						
K ₂ O	2.23	1.99	1.99	1.99	2.36	1.97	2.49	2.16	0.96	1.79	2.32	1.58	2.41	2.50	2.27						
P ₂ O ₅	0.81	0.63	0.83	0.85	0.93	0.70	0.86	0.88	0.58	0.63	0.69	0.63	0.87	0.96	0.82						
S	0.18	0.11	0.08	0.04	0.13	0.11	0.16	0.17	0.00	0.08	0.12	0.06	0.10	0.06	0.05						
Cl	0.07	0.06	0.02	0.03	0.06	0.05	0.08	0.07	0.00	0.02	0.05	0.03	0.07	0.06	0.05						
Total	98.37	98.80	98.36	99.22	98.74	98.30	98.69	98.42	99.53	99.25	98.74	98.82	97.64	96.81	97.08						
Cr ₂ O ₃	0.197	0.191	0.186	0.164	0.182	0.133	0.173	0.173	0.117	0.175	0.158	0.183	0.147	0.125	0.077						
NiO	0.045	0.054	0.048	0.046	0.042	0.031	0.039	0.070	0.058	0.036	0.038	0.038	0.027	0.054	0.070						
H ₂ O (SIMS)	—	—	—	—	—	—	—	0.7	0.0	—	—	—	—	1.1	1.6						
Major elements in olivine host, wt. %																					
Fo	88.46	87.70	86.83	87.22	88.02	90.75	88.87	88.43	89.46	90.64	90.31	91.20	92.14	92.36	92.26						
SiO ₂	40.52	40.11	40.23	40.26	40.74	40.39	40.52	40.42	40.54	40.50	40.54	40.18	40.57	40.99	40.66						
TiO ₂	0.041	0.038	0.049	0.041	0.052	0.042	0.036	0.032	0.035	0.061	0.039	0.038	0.042	0.035	0.041						
Al ₂ O ₃	0.046	0.031	0.035	0.029	0.035	0.052	0.037	0.048	0.048	0.063	0.056	0.048	0.058	0.064	0.065						
FeO	11.18	11.81	12.59	12.25	11.63	8.89	10.78	11.20	10.29	9.06	9.43	8.52	7.69	7.49	7.58						
MnO	0.183	0.189	0.208	0.205	0.192	0.160	0.183	0.192	0.179	0.149	0.150	0.139	0.129	0.129	0.127						
MgO	48.08	47.25	46.55	46.89	47.93	48.88	48.29	48.01	48.98	49.22	49.31	49.57	50.59	50.78	50.66						
CaO	0.460	0.581	0.546	0.566	0.494	0.539	0.457	0.479	0.453	0.376	0.374	0.328	0.359	0.354	0.354						
NiO	0.344	0.326	0.324	0.328	0.340	0.352	0.347	0.336	0.345	0.397	0.390	0.402	0.400	0.396	0.400						
CoO	0.021	0.023	0.022	0.023	0.020	0.018	0.020	0.021	0.021	0.018	0.017	0.018	0.015	0.016	0.014						
Cr ₂ O ₃	0.065	0.084	0.038	0.038	0.046	0.065	0.065	0.061	0.074	0.129	0.091	0.112	0.110	0.103	0.104						
Total	100.95	100.44	100.59	100.63	101.47	99.38	100.73	100.79	100.97	99.97	100.40	99.37	99.96	100.35	100.00						

Table 3 (continued)

Component	G-1-32*		G-1-32		G-1-32		G-1-32		G-1-32		G-1-32		G-3 (2994)		G-3 (2994)		G-1-25		G-1-25		
	70**	80	120	70	80	80	90	70	70	70	70	60	70	70	70	70	30	30	150	150	
	G1-32-3***		G1-32-4		G1-32-7		G1-32-9		G1-32-16		G1-32-22		G1-32-23		G1-32-1		G1-32-2a		G1-25-1a		
Trace elements and REE in melt inclusions, ppm																					
Rb	61.2	46.0	43.6	51.9	71.3	45.4	58.8	49.6	9.4	48.6	56.9	41.1	59.2	52.7	47.4						
Ba	838	720	655	775	938	752	837	690	606	663	743	556	972	847	745						
Th	8.27	7.84	8.07	8.41	9.60	8.82	9.66	7.86	5.93	9.49	9.65	6.75	10.34	7.54	6.87						
U	2.52	2.17	1.95	2.60	3.02	2.32	2.61	2.14	1.56	2.66	2.72	1.96	2.66	2.09	1.81						
Nb	107	98	94	106	124	99	112	98	78	119	126	84	121	106	91						
Ta	6.36	5.90	5.91	6.22	7.36	6.13	7.21	6.09	4.85	7.53	7.57	5.26	7.78	6.40	5.73						
La	87.2	82.6	81.7	90.6	99.3	86.5	96.6	82.5	66.5	99.7	102.7	71.5	102.1	87.3	73.6						
Ce	210	177	173	217	242	193	216	182	149	235	210	163	222	185	157						
Pb	8.79	7.18	6.97	8.36	9.09	8.23	8.85	6.51	0.10	7.67	8.88	6.21	10.04	5.73	11.22						
Pr	24.1	19.9	21.8	24.5	27.6	23.1	26.0	22.3	19.2	26.8	23.0	20.2	25.3	23.1	19.1						
Nd	97.3	77.5	90.3	92.8	111.1	92.8	105.6	93.3	81.8	106.5	88.2	82.7	101.8	93.5	79.0						
Sr	1195	1216	1119	1219	1282	1175	1261	1119	1083	1283	1320	944	1404	1301	1114						
Sm	17.6	13.6	16.2	15.7	19.5	15.9	18.0	17.4	15.8	18.2	15.2	15.4	17.5	16.7	13.8						
Zr	475	339	487	415	542	411	497	517	478	493	393	391	498	488	418						
Hf	10.5	8.2	11.3	9.5	13.2	9.7	11.8	12.3	11.7	12.2	9.2	9.2	12.1	12.8	10.1						
Eu	5.55	4.12	4.74	4.65	5.65	4.87	5.38	4.69	4.69	5.43	4.58	4.89	5.17	5.11	3.99						
Ti	34752	25608	32109	31586	38459	28378	34439	36347	38747	38690	31890	32342	34292	37068	32346						
Gd	13.5	11.3	12.8	11.5	15.8	12.4	14.0	12.6	13.4	14.5	12.8	12.9	13.5	13.2	10.5						
Tb	1.79	1.36	1.52	1.43	1.85	1.44	1.59	1.36	1.59	1.77	1.55	1.61	1.65	1.55	1.28						
Dy	8.88	6.95	7.63	7.08	8.58	7.09	8.25	7.11	7.80	8.62	7.06	8.69	8.16	7.47	6.41						
Ho	1.28	1.13	1.21	1.16	1.34	1.12	1.22	1.16	1.36	1.34	1.24	1.33	1.31	1.12	1.05						
Y	28.8	25.7	28.1	27.3	27.2	24.9	29.2	27.6	30.8	29.9	27.8	28.5	29.0	30.2	25.3						
Er	2.67	2.32	2.57	2.50	2.55	2.32	2.61	2.49	2.88	2.77	2.66	2.70	2.79	2.62	2.34						
Tm	0.28	0.29	0.28	0.26	0.30	0.27	0.31	0.28	0.42	0.38	0.32	0.31	0.35	0.19	0.29						
Yb	1.57	1.64	1.84	1.62	1.60	1.68	1.66	1.97	2.29	2.30	2.01	2.03	1.82	2.29	1.57						
Lu	0.17	0.20	0.24	0.19	0.18	0.21	0.20	0.22	0.22	0.25	0.22	0.24	0.27	0.27	0.23						
V	386	398	327	439	362	350	407	380	403	478	465	467	495	483	426						
Sc	22.6	24.7	29.1	25.8	27.5	29.7	32.7	32.5	42.6	48.5	37.0	36.6	40.5	53.0	33.3						
Li	11.9	14.6	9.2	14.2	15.0	39.1	8.84	9.85	7.77	7.94	6.79	7.13	6.72	9.64	5.34						

*, Sample; **, inclusion size, μm ; ***, sampling site.

CaO, in the meimechite olivine are much higher than those in WPM, MORB, and komatiites. The NiO contents are, on the contrary, lower than in magnesian olivine of typical WPM and komatiites approaching those in most magnesian olivine from MORB. Cr₂O₃ are higher than in MORB olivine but lower than in magnesian olivine from WPM, and especially from komatiites.

The analyzed olivine phenocrysts in meimechites differ strongly from those in the Gudchikhinskaya suite picrites (Fig. 5) which erupted in the beginning of the flood volcanic event of the Siberian Trap Province (Fedorenko et al., 1996; Lightfoot et al., 1993; Sobolev, et al., 2009a). The latter have notably lower Mg# and contain less CaO and Cr₂O₃, but have similar concentrations of NiO relative to the former.

Compared with olivines in mantle-derived rocks of the Siberian craton (Sobolev, et al., 2008b, 2009b), those in meimechites have obviously higher CaO (above 0.29 wt.% against below 0.12 wt.%).

Melt inclusions

High crystallization temperatures (above 1450 °C) of meimechites were first inferred from homogenization of melt inclusions in olivine (Sobolev et al., 1972). Later special studies of homogenization temperatures and major-element compositions of melt inclusions in olivine phenocrysts from meimechites (Sobolev and Slutskii, 1984; Sobolev et al., 1991) supported that inference having constrained the olivine crystallization temperatures to a range of 1600–1420 °C, and revealed a strong positive correlation between homogenization temperature of melt inclusions and Mg# of the olivine host. In this paper we report new data on concentrations of major, trace, and volatile elements in melt inclusions from meimechite olivine phenocrysts (Fig. 7).

Melt inclusions were quenched at temperatures much below the temperature of complete homogenization but above the melting point of latest clinopyroxene crystals. The quenched inclusions consisted of bright brown glass, a large spherical gas phase (shrinkage bubble, Fig. 7), and Cr spinel (Fig. 7, c, d). The shrinkage bubble had a low refractive index, showed no phase boundaries at room temperature and, hence, had a low density.

Composition of trapped melt: major elements. The composition of glass in quenched melt inclusions (Table 3) differs from the primary composition of trapped melt as a result of olivine crystallization on inclusion walls and inclusion-host exchange of elements (Danyushevsky et al., 2000, 2002; Portnyagin et al., 2008; Sobolev and Danyushevsky, 1994; Sobolev and Slutskii, 1984; Spandler et al., 2007). The respective crystallization and FeO–MgO exchange corrections require knowledge of the initial FeO content in the entrapped melt (Sobolev and Danyushevsky, 1994), which was estimated by simulating crystallization of aphyric meimechite from the aphanite margin of a meimechite dike (sample 1205a from (Sobolev and Slutskii, 1984)). The sample was free from olivine phenocrysts because they moved into the dike center

with olivine-liquid flow and thus represented meimechite magma at the onset of crystallization.

In order to infer the primary magma composition, the whole-rock chemistry of sample 1205a corrected for Na loss (see below) was modeled as the reverse of fractional crystallization till equilibrium with the most magnesian olivine Fo₉₃ (Arndt et al., 1998; Sobolev and Slutskii, 1984; Sobolev et al., 1991). The next step was to model fractional crystallization till equilibrium with Fo₈₆ olivine, for an oxygen fugacity of QFM + 1.5, according to oxygen fugacity at crystallization of meimechites (see below). The olivine–liquid equilibrium was calculated using models of Ford et al. (1983) and Herzberg and O'Hara (2002) which provide the best account of high-temperature heating experiments (Falloon et al., 2007). The iron oxidation degree in the liquid was determined using models of Sack et al. (1980) and Borisov and Shapkin (1989) which better fit the experimental data for oxidized conditions (Danyushevsky and Sobolev, 1996).

Comparison of the modeling results (Fig. 8) with those of experimental homogenization of melt inclusions (Sobolev et al., 1991) showed the latter to lie between the predicted trends and to fit better the models of Herzberg and O'Hara (2002) and Borisov and Shapkin (1989). Additional check of the estimated FeO contents in the meimechite magma was against the compositions of rocks (Fig. 9) which are composed of melt and olivine and thus must have their MgO–FeO within the ABCD domain in the diagram of Fig. 9. This condition is satisfied by 94% of published meimechite compositions, with a 5% error. Note that FeO in homogenized melt inclusions in olivine from meimechites, as well as in most of olivine porphyric rocks, are systematically lower due to FeO–MgO exchange between the host olivine and the entrapped liquid (Sobolev and Danyushevsky, 1994). Thus, the modeled crystallization path based on (Borisov and Shapkin, 1989; Herzberg and O'Hara, 2002), being consistent with experimental data (Fig. 8) and with whole-rock compositions (Fig. 9), is applicable to estimate the initial FeO content in melt inclusions.

The obtained relationship between total iron (as FeO) in the liquid and in the equilibrium olivine was parameterized as

$$(\text{FeO})_{\text{tot}} = -0.026(\text{Fo})^2 + 4.3077\text{Fo} - 161 \quad (R^2 = 0.9999), \quad (1)$$

and this equation was then used to determine the initial total iron in trapped melt inclusion from the host olivine composition.

In order to consider the effect of near-surface degassing on the meimechite magma composition, we analyzed the composition of an inclusion which fully opened during an optically controlled high-temperature run (G1-32-2a, Table 3) as a result of olivine wall melting at 1350 °C. The inclusion was quenched after being exposed to that temperature for 5 minutes, and its composition was calculated following the same procedure as for the closed inclusions.

The compositions of quenched melt inclusions were recalculated till equilibrium with the host olivine using initial FeO found by (1) (Table 4). The same modeling procedure was applied to quenched melt inclusions in meimechite olivines

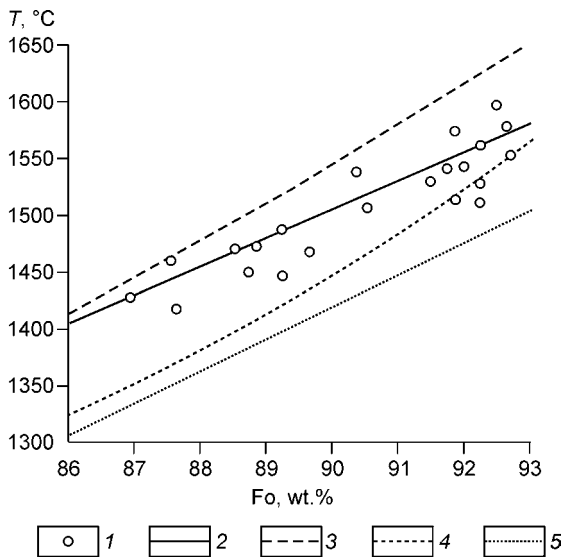


Fig. 8. Homogenization of melt inclusions in olivine from meimechites and model crystallization path of meimechite magma. 1, homogenization temperatures (Sobolev et al., 1991); 2, fractionation of meimechite magma (sample 1205a, see text) at oxygen fugacity corresponding to QFM + 1.5, based on models by Borisov and Shapkin (1989) and Herzberg and O'Hara (2002); 3, same, based on models by Sack et al. (1980) and Herzberg and O'Hara (2002); 4, same, based on models by Sack et al. (1980) and Ford et al. (1983); 5, same, based on models by Ford et al. (1983) and Borisov and Shapkin (1989).

reported in (Ryabchikov et al., 2009). The modeled trapped liquid compositions were then compared with those of homogenized melt inclusions in olivines (Fig. 10).

The entrapped meimechite melt was inferred to have a highly magnesian, ultramafic, and alkaline composition. Most elements in both inclusions and rocks followed the trend of crystallization or accumulation of magnesian olivine, except K and especially Na. Note that whole-rock Na (in a majority of rocks) and K (in one third of rocks) are systematically lower than in melt inclusions. This effect was reported earlier for meimechites (Sobolev and Slutski, 1984; Sobolev et al., 1991) and was attributed to loss of alkalis during late-magmatic or post-magmatic alteration of rocks. New data fully support this explanation.

The composition of the experimentally degassed inclusion (G1-32-2a, Table 3) differs significantly from that of sealed inclusions in lower K (about 40% of the norm) and Na (about 75%) (Fig. 10, Tables 3, 4). Thus, partial degassing during opening may be responsible for K depletion in some inclusions (Ryabchikov et al., 2009).

Oxygen fugacity at crystallization of meimechites.

Knowledge of redox conditions is necessary to quantify the $(\text{Fe}^{3+})/(\text{Fe}^{2+})$ ratios in the liquid in all models of olivine–liquid equilibrium. Oxygen fugacity (f_{O_2}) for meimechites, as inferred from the chemistry of coexisting olivine and spinel (Mungall et al., 2006; Ryabchikov et al., 2009; Sobolev and Slutski, 1984) or from V partitioning between olivine and liquid (Mungall et al., 2006), was two orders of magnitude above the QFM buffer. Slightly more reduced conditions (QFM–QFM + 1) were obtained (Sobolev et al., 1991) using spinel–liquid equilibrium. The new estimates of oxygen fugac-

ity at crystallization of meimechites presented here were based on V partition between olivine and trapped melt and on the model of Mallmann and O'Neill (2009).

Vanadium partition between the host olivine and the trapped meimechite melt (Table 4) is shown in Fig. 11, a together with the similar data for tholeiitic picrites of the Hawaiian plume (shield stages of Koolau, Mauna Loa, and Mauna Kea volcanoes) and subalkaline picrites of the post-shield stage of Mauna Kea (unpublished data by A.V. Sobolev). Oxygen fugacities at crystallization of the respective magmas inferred from the model of Mallmann and O'Neill (2009) are also shown. Meimechites obviously demonstrate lowest V partition coefficients and the highest f_{O_2} corresponding to QFM + 1.5 \pm 0.5. This estimate is similar to those reported in (Mungall et al., 2006; Ryabchikov et al., 2009; Sobolev and Slutski, 1984) and is 0.5–1.5 orders of magnitude higher than that in (Sobolev et al., 1991). The latter f_{O_2} (Sobolev et al., 1991) may be, however, underestimated because of systematic deviation of the high-Ti spinel–liquid equilibrium from the experimental equilibrium determined for lower-Ti systems (Danyushevsky and Sobolev, 1996; Maurel and Maurel, 1982).

According to f_{O_2} (Fig. 11, b) inferred from the V/Sc ratio in the melt (Mallmann and O'Neill, 2009), most magmas were originally generated in more reduced conditions than they later crystallized. The systematic f_{O_2} shift is the greatest (about two orders of magnitude) for meimechite and other alkaline magmas, such as postshield Mauna Kea.

Composition of trapped melt: volatiles. In addition to S and Cl determined by EPMA, we have obtained first SIMS

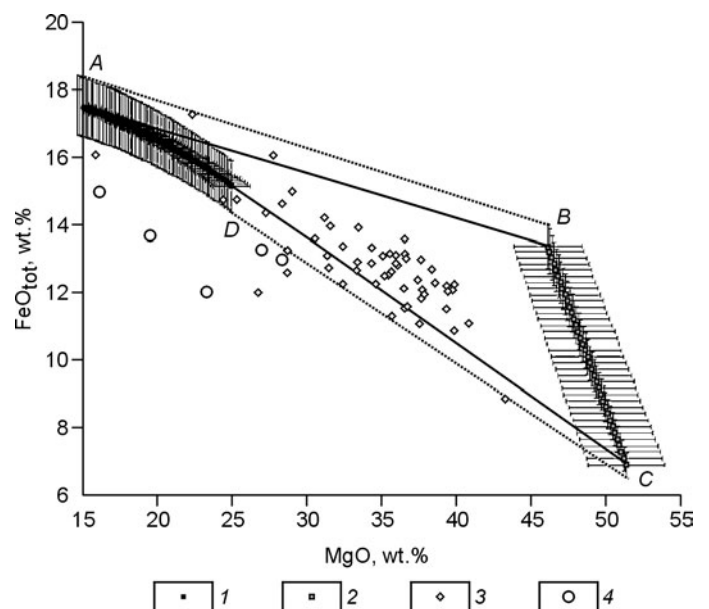


Fig. 9. Predicted paths of liquid (1) and equilibrium olivine (2) during fractionation of meimechite primary magma (sample 1205a, see text), compared with compositions of meimechite rocks (3), after (GEOROC <http://georoc.mpch-mainz.gwdg.de/georoc/>), and homogenized melt inclusions (4), after (Sobolev et al., 1991).

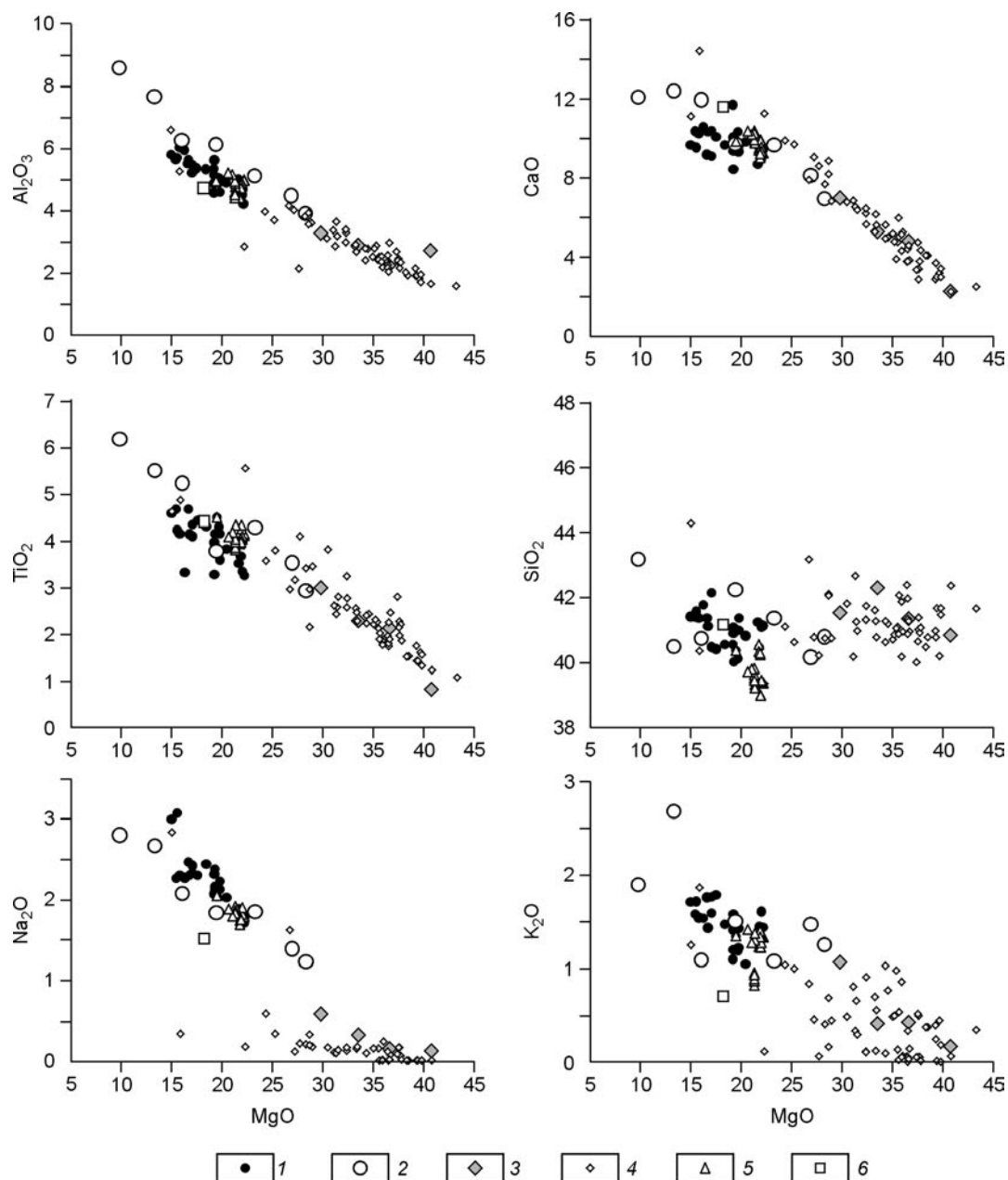


Fig. 10. Meimechite melt entrapped in olivine phenocrysts. 1, predicted composition of entrapped melt; 2–6, compositions of homogenized inclusions in olivine (Sobolev et al., 1991) (2), analyzed rock samples (3), meimechites, from published evidence (Fig. 3) (4), trapped melt, calculated according to (Ryabchikov et al., 2009) (5), artificially degassed inclusion (G1-32-2a, Table 3) (6).

data on H₂O contents in meimechite magma. The measured contents of volatiles in melt inclusions (Table 3) were recalculated to the trapped liquid composition assuming their zero concentrations in the olivine host.

The S and Cl abundances are found to vary in a broad range (Table 4, Fig. 12, *a*) and correlate at $R^2 = 0.71$ with their ratio being stable at $S/Cl = 2.1 \pm 0.2$ (standard error) and thus indicating incompatible behavior of both elements. However, the correlation of Cl with K is much weaker ($R^2 = 0.41$) with K/Cl ratio being variable. The S-K correlation is

insignificant, and S in melts is systematically below the sulfide liquid saturation (Fig. 12, *b*). Thus, S and Cl both show incompatible behavior but behave in a different way relative to nonvolatile incompatible elements. The contents of S and Cl in the degassed melt inclusion were below the detection limit (about 20 ppm).

The H₂O content was found to be from less than 0.02 wt.% in fully degassed melt to 0.6–1.1 wt.% in originally hermetic melt inclusions recalculated to equilibrium with the olivine host (Table 4). Correlation cannot be estimated quantitatively

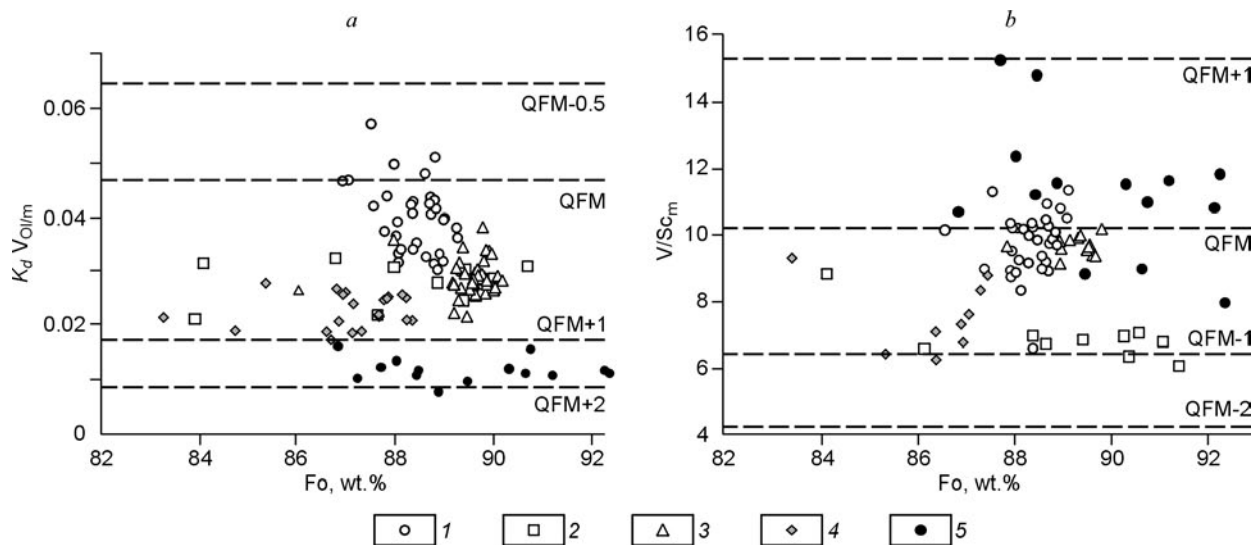


Fig. 11. Oxygen fugacity (a) during crystallization of mantle magmas, from olivine-liquid V partitioning and (b) during magma generation, from V/Sc ratio in melt (Mallmann and O'Neill, 2009). 1–4, Hawaiian picrites in Koolau volcano, shield stage (1), Mauna Loa volcano, shield stage (2), Mauna Kea volcano, shield stage (3), Mauna Kea volcano, post-shield stage (4); 5, meimechites.

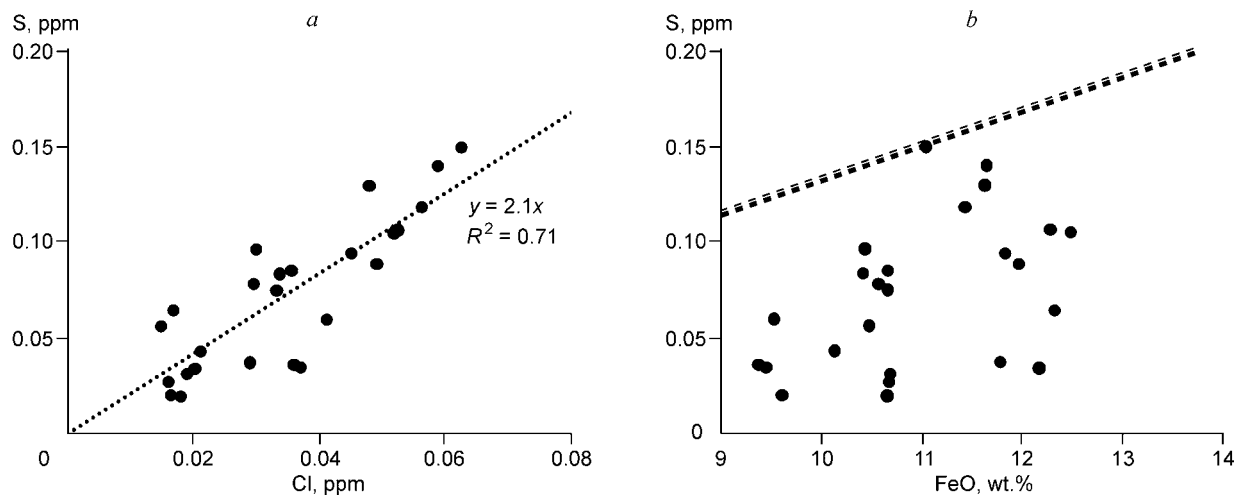


Fig. 12. Volatiles entrapped in meimechite melt. a, S–Cl diagram, dotted line shows linear regression according to given equation and correlation coefficient; b, S–FeO diagram (only Fe^{2+}), dashed line shows saturation of basaltic melt with sulfide melt (Mathez, 1976).

for the data shortage, but the variable $\text{H}_2\text{O}/\text{K}_2\text{O}$ and $\text{H}_2\text{O}/\text{Cl}$ ratios indicate independent behavior of water from elements with similar incompatibility with the solid.

Composition of trapped melt: trace elements. The measured trace-element abundances in melt inclusions (Table 3), except Sc and Li, were normalized to the entrapped liquid composition (Table 4), assuming zero concentrations in the host olivine. Sc and Li were recalculated with regard to their olivine–melt partitioning (coefficients 0.2 and 0.3) according to (Mallmann and O'Neill, 2009) and (Nikogosian and Sobolev, 1997), respectively. The normalized patterns of incompatible elements in entrapped melts (Fig. 13) show enrichment in most elements, as in the rocks, and depletion in typical garnet elements (HREE, Y, Sc, and Al) and in U, Th, and Rb relative to elements of similar incompatibility. Other features we observed are the quite strong depletion in

Pb compared with Ce and Pr and in K relative to La and Nb, Ta. Characteristic Ce/Pb and Nb/U indicate the absence of continental crust contamination in meimechite magma which in this respect approaches the least contaminated Siberian lavas (Fig. 14). Most elements have similar concentrations in the artificially degassed (G1-32-2a) and hermetically sealed melt inclusions, except Rb and Pb which are times as low in the former (about 16% Rb and 1% Pb) (Fig. 13).

Primary magma of meimechites

Major elements. The primary magma composition of meimechites (Table 5) was estimated by reversing fractional crystallization of olivine in entrapped melt to equilibrium with the most magnesian $\text{Fo}_{93.0}$ olivine of meimechites. For this

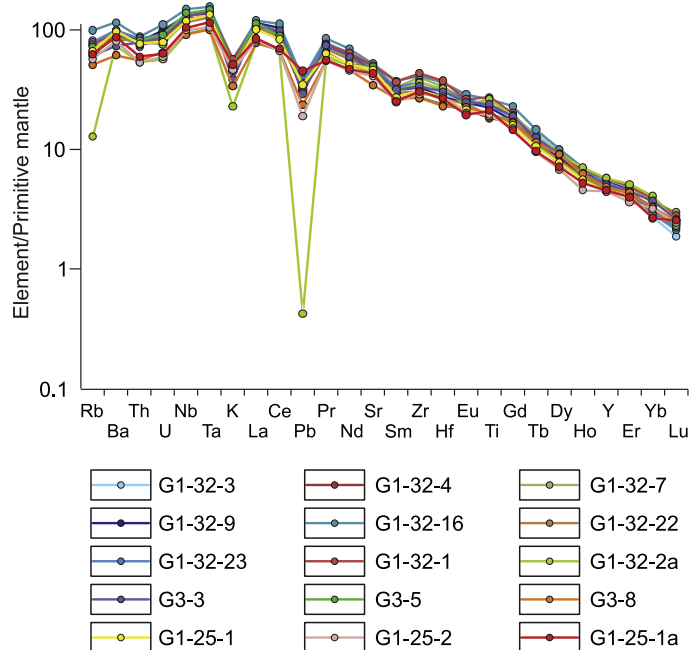


Fig. 13. REE patterns of melt inclusions in olivine from meimechites. Element abundances are normalized to primitive mantle (Hofmann, 1988).

purpose we used the olivine–liquid equilibrium model of Herzberg and O’Hara (2002) together with the model of iron oxidation in natural melts (Borisov and Shapkin, 1989) which provide the best account of homogenization temperatures of melt inclusions in olivine (Fig. 8). Oxygen fugacity was assumed to be at QFM + 1.5 (see below). The obtained MgO content is 24 wt.%, or somewhat lower than the previous estimates (26–29 wt.%) from (Arndt et al., 1995; Sobolev and Slutski, 1984; Sobolev et al., 1991).

Trace elements. Incompatible trace elements in the parental meimechite liquid (Table 5, Fig. 15) were inferred from their abundances in trapped melt by adding the required amount of olivine. In addition, we normalized the composition of the studied meimechite rocks to TiO₂ in the parental melt (Fig. 15). Both estimates show good agreement within an error of 20% for most elements except Rb, Ba, U, K, Pb, and Sr. It is seen from Fig. 15 that the artificially degassed meimechite melt perfectly simulates the difference in contents of these latter elements between rocks and hermetic melt inclusions. This suggests the composition change in the post-magmatic process and, on the other hand, gives more credit to data on hermetic inclusions.

The normalized patterns of incompatible elements in the parental meimechite magma are compared in Fig. 15 with those of the Gudchikhinskaya suite picrites (Norilsk area) erupted in the beginning of the flood-volcanic event. Although the slopes of the spectra differ significantly, the patterns show a striking similarity with almost coinciding peaks and dips, except for the Rb negative anomaly present in the meimechite magma but absent in the Gudchikhinskaya suite magma (Fig. 15).

Volatiles. Estimating the concentrations of volatiles in the parental liquid may be problematic due to difficulty in

accounting for the degassing process. The hardest point is to determine elements poorly soluble in melt at the pressure of crystallization, which was below 50 MPa for meimechites (Sobolev and Slutski, 1984). At this pressure one may expect degassing of almost all initial CO₂ and a large part of H₂O. That is why it is reasonable to infer initial CO₂ and H₂O contents according to the concentrations of nonvolatile elements that have similar incompatibility with the solid phase in the magmatic process: Nb for CO₂ and Ce for H₂O (Cartigny et al., 2008; Saal et al., 2002). Their characteristic ratios CO₂/Nb and H₂O/Ce in the meimechite magma were estimated to be 1000 and 170, respectively, from the La/Sm dependence reported by (Cartigny et al., 2008). For estimated primary meimechite melt this corresponds to CO₂ = 5.8 wt.% and H₂O = 1.8 wt.%. Note that for H₂O this estimate is only slightly above the measured maximum value, which corresponds to ~1 wt.% when recalculated to the parental liquid (Table 4). The latter contains within 0.06 wt.% S on average and about 0.03 wt.% Cl.

Source composition. According to A.V. Sobolev et al. (2005a, 2007), Ni enrichment and Mn depletion in olivine relative to the equilibrium with mantle peridotite indicate that the system contains melting products of the olivine-free pyroxenite produced by a reaction between recycled crust and peridotite. The Mn/Fe and Ni/(Mg/Fe) ratios in olivine were parameterized for estimating the fraction of pyroxenite-derived melt (Sobolev et al., 2007, 2008a). Olivines from the Gudchikhinskaya suite flood basalts show a large fraction of the pyroxenite component in their source (Sobolev et al., 2009a), whereas olivines in meimechites indicate an olivine-bearing (peridotite) source (see the respective olivine compositions

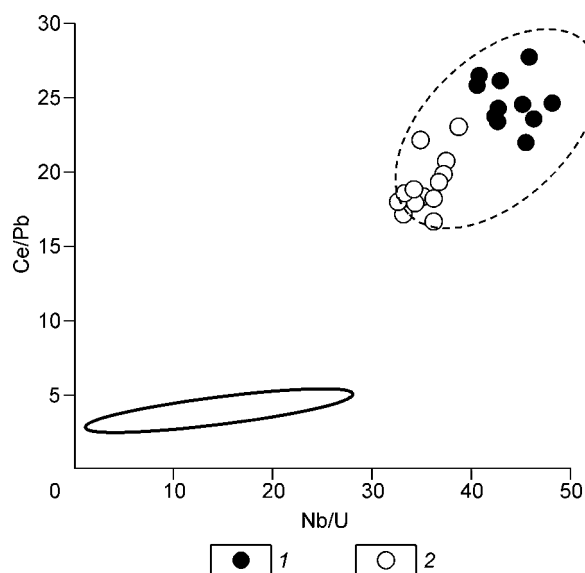


Fig. 14. Indicator trace-element ratios in melt inclusions in olivines from meimechites. Dashed line contours OIB field, according to (Hofmann, 2002) and GEOROC database (<http://georoc.mpch-mainz.gwdg.de/georoc/>). Solid line contours field of crystalline rocks of continental crust (Rudnick, 2002). 1, melt inclusions in olivines from meimechites; 2, least contaminated Gudchikhinskaya suite magmas (Sobolev et al., 2009a).

Table 5
Meimechite primary magma

Melt	SiO ₂	TiO ₂	Al ₂ O ₃	Fe ₂ O ₃	FeO	MnO	MgO	CaO	Na ₂ O	K ₂ O	P ₂ O ₅	Cr ₂ O ₃	NiO	H ₂ O	CO ₂	S	Cl	T _d 0	
Dry	40.97	3.30	4.26	6.22	9.18	0.15	24.00	8.16	1.77	1.26	0.47	0.11	0.134	0.00	0.00	0.00	0.00	0.00	1570
With volatiles	37.81	3.05	3.94	5.74	8.48	0.14	22.15	7.53	1.63	1.16	0.43	0.10	0.124	1.8	5.8	0.06	0.03	—	—
Rb	Ba	Th	U	Nb	Ta	La	Ce	Pb	Pr	Nd	Sr	Sm	Zr	Hf	Eu	Ti	Gd		
28.5	418	4.64	1.29	57.9	3.56	48.4	108	4.45	12.7	51.1	660	8.99	248	5.93	2.68	18 255	7.06		
Tb	Dy	Ho	Y	Er	Tm	Yb	Lu	Sc	Zr	Li	V	T _d 6.0	T _d 8.0	T 6.0	T 8.0	T _p 6.0	T _p 8.0		
0.85	4.20	0.66	15.2	1.40	0.16	1.00	0.12	21.0	248	7.88	228	1822–1906	1906–2018	1612–1696	1696–1808	1552–1636	1636–1728		

Note. T_d is predicted dry temperature (°C) at pressures 6 and 8 GPa, respectively; T is predicted temperature with regard to volatiles at pressures 6 and 8 GPa, respectively; T_p is predicted potential temperature with regard to volatiles at pressures 6 and 8 GPa, respectively. Maximum temperature estimate corresponds to liquidus slope of 0.56 °C/GPa (Ford et al., 1983), minimum temperature estimate to liquidus slope of 0.42 °C/GPa (Herzberg, O'Hara, 2002).

compared in Fig. 16). This inference is consistent with high MgO contents in meimechite primary magma. Furthermore, the concentration of Cr in olivines, which is lower in meimechites than in komatiites (Fig. 5), also indicates a significant percentage of Cr-rich garnet in the meimechite melting residue.

Petrology of meimechites

Potential mantle temperature. Following the pioneering study by V.S. Sobolev et al. (1972), most workers engaged in meimechite studies agree about exceptionally high temperatures of emplacement (eruption) of meimechite magma at shallow depths, which may have reached 1600–1580 °C at pressures below 50 MPa (see Sobolev and Slutskii, 1984 ; Sobolev et al., 1991, and this study). Meimechite magma evidently originated at ultrahigh pressures of ~6–8 GPa (Arndt et al., 1995; Elkins-Tanton et al., 2007; Ryabchikov et al., 2009; Sobolev et al., 1991) and temperatures of 1820–2020 °C, as one may estimate assuming that meimechite melt has not changed in composition since its eruption and the liquidus slope has been 0.42 °C/GPa (Herzberg and O'Hara, 2002) or 0.56 °C/GPa (Ford et al., 1983) (see Table 5). Converted to the potential mantle temperature (McKenzie and Bickle, 1988), these values correspond to 1760–1940 °C, which are more than 150 °C hotter than the highest potential temperature of Phanerozoic mantle (Herzberg and Gazel, 2009) and of the Siberian mantle plume (Sobolev et al., 2009a). This result is obviously problematic and causes reasonable doubt (Elkins-Tanton et al., 2007).

New data on volatiles in meimechite primary magma, with 5.8 wt.% CO₂ and 1.8 wt.% H₂O, imply much lower temperatures of its generation. The cooling effect of this amount of H₂O estimated with reference to (Falloon and Danuyshevsky, 2000) is 90 °C, and the effect of CO₂ can be inferred from experimental results of Dasgupta et al. (2007). The CO₂ dependence of the difference between experimentally measured (with CO₂) and computed “dry” liquidus temperatures at 3 GPa which is plotted in Fig. 17 shows a strong positive correlation and indicates possible cooling of ~120 °C due to 6 wt.% of CO₂. The total cooling effect of volatiles (CO₂ plus H₂O) thus exceeds 210 °C and leads to a potential mantle temperature of 1550–1730 °C or 1640 ± 90 °C (Table 5). Inasmuch as all CO₂ and a large part of H₂O leave the rising magma at high-pressure depths, the erupted melt must be almost “dry” and have a temperature below 1570 °C.

Relation to Gudchikhinskaya suite flood basalts. The predicted potential temperature of meimechite magma (1640 ± 90 °C) is much above that of convecting upper mantle (1350 °C according to McKenzie and Bickle (1988)) and, hence, is consistent with a plume-associated origin of meimechites (Arndt et al., 1995; Basu et al., 1995; Dobretsov et al., 2008; Ryabchikov, 2003; Ryabchikov et al., 2009; Sobolev et al., 1991). Relation of meimechites to the Siberian plume is further supported by the proximity of this temperature to that in the beginning of the flood volcanic event (at least

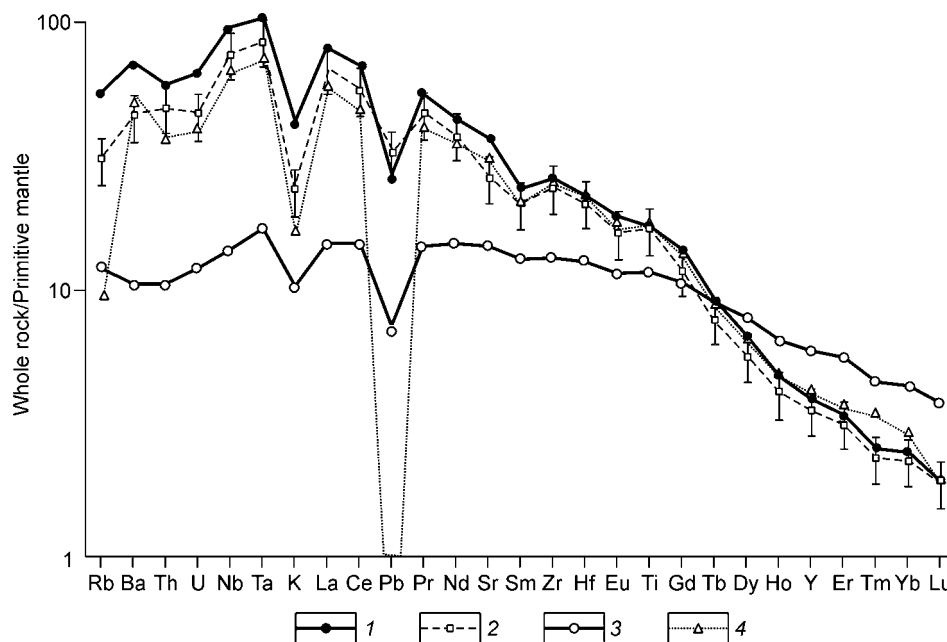


Fig. 15. REE patterns of primary magmas of meimechites and Gudchikhinskaya suite traps. 1, meimechite primary magma, predicted from compositions of melt inclusions; 2, TiO₂-normalized (3.05 wt.% TiO₂) composition meimechite primary magma, predicted from compositions of meimechites; error bars correspond to $\pm 20\%$; 3, primary magma of Gudchikhinskaya suite picrites (Sobolev et al., 2009a); 4, TiO₂-normalized (3.05 wt.% TiO₂) composition of degassed melt inclusion in olivine from meimechites (G1-32-2a, Tables 3 and 4). Element abundances are normalized to primitive mantle (Hofmann, 1988).

1540 \pm 40 °C) (Sobolev et al., 2009a). Additional evidence for this hypothesis, besides the geological setting and age of meimechites, comes from their isotope signature similarity with noncontaminated Gudchikhinskaya suite picrites, namely, high ϵ_{Nd} (up to 6) and low $^{87}\text{Sr}/^{86}\text{Sr}$ (below 0.7032) (Arndt et al., 1995, 1998; Carlson et al., 2006; Kogarko et al., 1988; Lightfoot et al., 1993; Wooden et al., 1993), as well as the similarity in the patterns of incompatible elements in the Gudchikhinskaya suite and meimechite primary magmas (Fig. 15).

Petrogenesis of meimechites. The petrogenetic model of meimechites should explain the high contents of incompatible elements, including CO₂ and H₂O, together with high MgO contents and presence of garnet and olivine in the mantle source. It also should account for the K and Rb negative anomalies and for the similarity of meimechite and flood basalts the patterns in Fig. 15. Finally, it should provide explanation for the weakly fractionated pattern PGE and S depletion in meimechites (Fig. 12, b) implying the absence of the residual sulfide phase (Mungall et al., 2006) and high oxidation of crystallizing melt (Fig. 11, a).

Low-degree partial melting of peridotite is a classic model for melt enrichment in incompatible elements in which the combination of low melting degree with high MgO and garnet signatures in the meimechite composition is easily explained by high pressures (6–8 GPa) of peridotite melting (Arndt et al., 1995; Elkins-Tanton et al., 2007; Ryabchikov et al., 2009; Sobolev et al., 1991). This idea is also consistent with high CO₂ and H₂O which behave as strongly incompatible elements at high pressures, and with the presence of olivine in the source (Fig. 16). Furthermore, it can account for the K and, possibly, also Rb minimums in meimechites (Fig. 15) due to

incorporation of K (Rb) into residual clinopyroxene at high pressures (Perchuk et al., 2000; Safonov et al., 2005; Sobolev, 1974).

However, low-degree partial melting of peridotite is expected to leave a sulfide phase in the residue and, hence,

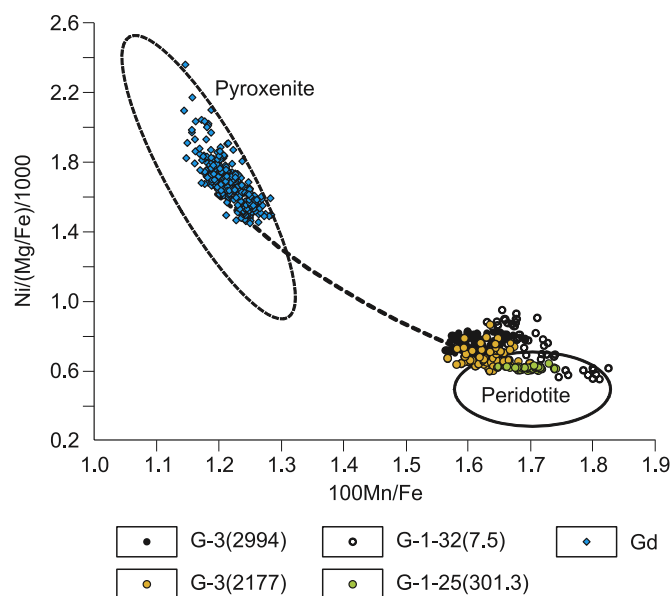


Fig. 16. Phase composition of mantle source, according to Ni enrichment and Mn depletion in olivine phenocrysts (Sobolev et al., 2007). Symbols show compositions of olivine from samples of meimechite and Gudchikhinskaya suite picrites (Gd). Contoured are fields of olivine equilibrium with typical peridotite- and pyroxenite-derived liquids. Mixing line of boundary components (dashed line) is according to model of Herzberg and O'Hara (2002).

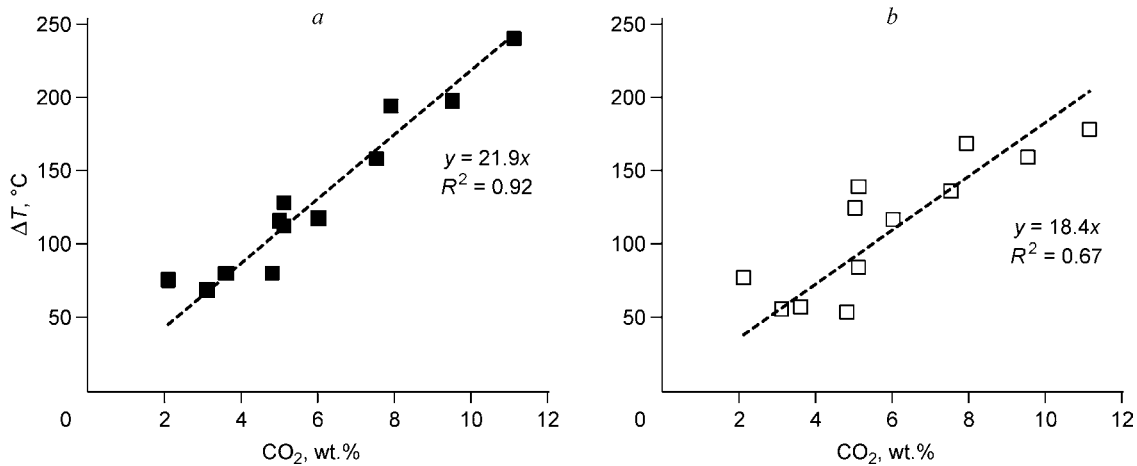


Fig. 17. CO₂ dependence of liquidus temperature of silicate melts at 3 GPa, after experimental data reported in (Dasgupta et al., 2007). CO₂ contents are estimated from mass balance (Dasgupta et al., 2007). Figures are regression equations and correlation coefficients. *a*, Difference between dry liquidus temperature according to model of Ford et al. (1983) and experimental temperature; *b*, difference between “dry” liquidus temperature according to model by Herzberg and O’Hara (2002) and experimental temperature.

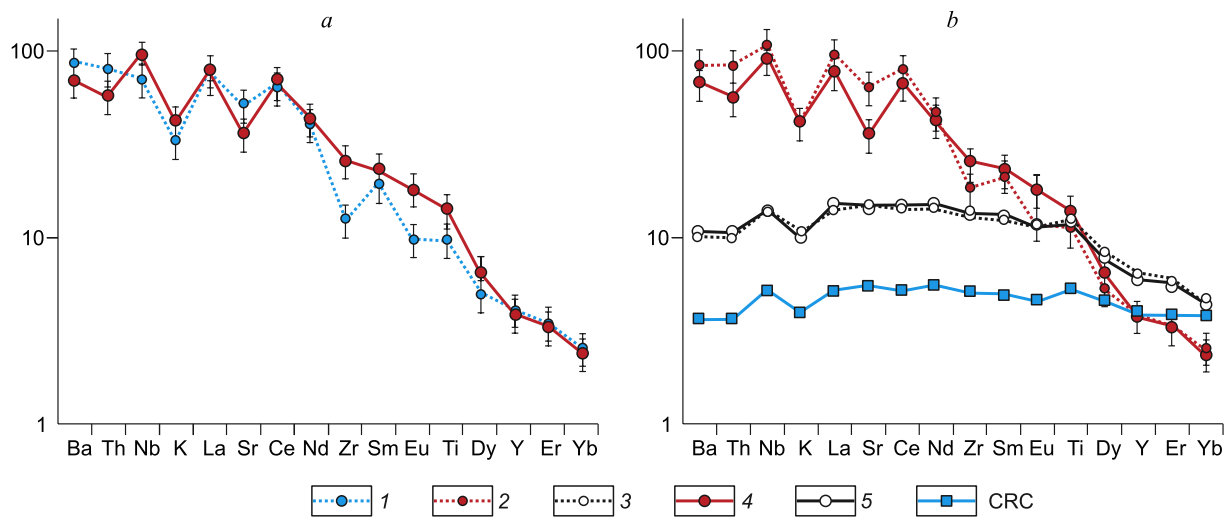


Fig. 18. Modeled generation of primary magmas of meimechites and Gudchikhinskaya suit picrites. *a*, Failed modeling; *b*, successful modeling. Element abundances are normalized to primitive mantle (Hofmann, 1988). Numbers and abbreviations as in Table 6: 1, product of 1.5% partial melting of primitive mantle garnet peridotite (PM, Table 6); 2, product of 11% partial melting of depleted garnet harzburgite (DM, Table 6), metasomatized by 10% of carbonate-silicate melt that results from 5% partial melting of recycled crustal component as eclogite (CRC); 3, product of 40% partial melting of reaction pyroxenite (60% partial melt of recycled eclogite (CRC) and 40% primitive mantle peridotite (PM, Table 6)); 4, meimechite primary magma; 5, primary magma of Gudchikhinskaya suit picrites (Sobolev et al., 2009a)

induce considerable PGE fractionation. The lack of this effect in meimechites has been attributed to high oxygen fugacity during their melting which would cause oxidation of sulfur into the sulfate form and its dissolution in the melt (Mungall et al., 2006). Although meimechites had high oxygen fugacity at shallow crystallization depths (Fig. 11, *a*), their source not necessarily was as oxidized: oxidation may have occurred during decompression degassing on the way to the surface (Mathez, 1984). One can check the primary oxidation of the meimechite source according to the V/Sc ratio in the melt using experimental data from (Mallmann and O’Neill, 2009). The V/Sc ratios in meimechite magma are similar to those in

other magmas and correspond to f_{O_2} about the QFM buffer (Fig. 11, *b*), i.e., oxidation of the mantle source was normal, and the absence of sulfide in the residue must have a different reason.

The single-stage formation model of meimechites implying low-degree melting of peridotite faces another problem which shows up in quantitative modeling (Fig. 18, *a*). This model assuming 1–2% melting of various mixtures of primitive and depleted mantle can account for the given abundances of most (LREE, Nb, K, Th, Ba) and least (HREE and Y) incompatible trace elements, but the concentrations of Ti, Eu, and Zr are inconsistent with this idea (e.g., it accounts for no more than

Table 6. Parameters of melting modeling

Elements	PM	CRC	DM		1	2	3	4	5
Ba	1	3.64	0.084		86.03	84.4	10.23	69.1	10.6
Th	1	3.69	0.051		79.70	84.2	10.36	57.1	10.6
Nb	1	5.18	0.043		71.04	108.9	14.15	93.7	14.2
K	1	4.00	0.000		32.77	41.4	10.87	41.9	10.3
La	1	5.21	0.120		72.67	97.6	14.23	78.9	15.0
Sr	1	5.49	0.149		51.37	64.7	14.93	36.3	14.7
Ce	1	5.31	0.025		63.24	79.9	14.47	67.6	15.0
Nd	1	5.47	0.059		40.22	46.9	14.86	43.0	15.0
Zr	1	5.15	0.238		12.50	18.7	13.30	25.5	13.3
Sm	1	4.92	0.039		19.27	21.7	13.13	23.3	13.1
Eu	1	4.65	0.037		9.68	12.1	11.49	18.4	11.6
Ti	1	5.38	0.093		9.73	11.1	12.37	14.0	11.7
Dy	1	4.70	0.086		4.94	5.5	8.41	6.6	8.0
Y	1	4.06	0.110		4.08	4.0	6.59	3.9	6.0
Er	1	3.84	0.106		3.50	3.3	5.86	3.4	5.7
Yb	1	3.86	0.161		2.55	2.6	4.63	2.4	4.4
Phases	Model parameters				Primary melts				
CO	0	0.09	0						
OL	0.52	0.00	0.76	FCRC	no	0.05	0.60		
OPX	0.28	0.00	0.21	XCRC	0	0.10	0.60		
CPX	0.1	0.56	0.01	M	PM	DM	PM		
GA	0.1	0.35	0.02	F	0.02	0.11	0.40		

Note. Composition numbers correspond to Fig. 18, all compositions are normalized to PM, primitive mantle (Hofmann, 1988); CRC, crustal recycled component; DM, depleted mantle (depleted abyssal harzburgite from South West Indian Ridge, sample Prot 34D-1 (Niu, 2004). Phases: CO, coesite; OL, olivine; OPX, orthopyroxene; CPX, clinopyroxene; GA, garnet. Model parameters: FCRC, melting fraction of CRC; XCRC, amount of CRC, derived melt in reaction product; M, type of mantle component in reaction product; F, melting fraction of reaction product. Melting reaction as in (Sobolev et al., 2005a) and partition coefficients as in (Sobolev et al., 2000), except coefficient for K partition between CPX and melt, which was set here at 0.2 (instead of 0.1 in (Sobolev et al., 2000)) in account for high pressure affect (Perchuk et al., 2000; Safonov et al., 2005).

70% of Ti, Fig. 18, *a*). The problem of Ti concentrations in mantle magmas, and specifically in meimechites, was discussed before in (Kogarko and Ryabchikov, 2000; Prytulak and Elliott, 2007). Namely, Prytulak and Elliott (2007) proved, proceeding from Ti partitioning between mantle minerals and melt, that TiO₂ in melts of primitive mantle not exceed 2–2.5% at lowest melting degrees, which is much lower than in meimechite primary magma (Table 5).

In addition, the single-stage model fails to explain the trace-element similarity of meimechite primary magma to that of the Gudchikhinskaya suite picrites which was derived from a pyroxenite mantle source and gave rise to flood volcanics in the Norilsk area (Sobolev, et al., 2009a). The problem is that the patterns of incompatible elements in the Gudchikhinskaya suite parental magma bear signatures of recycled oceanic crust (see Fig. 18, *b* and (Sobolev, et al., 2009a)), i.e., oceanic crust may have played some role in the origin of meimechites as well.

We suggest to overcome these problems using a model of three-stage formation of meimechites. We assume that mantle peridotite, the source of meimechite magma, was previously metasomatized with a carbonate-silicate melt which, in turn,

resulted from low-degree partial melting of carbonated eclogite associated with recycled oceanic crust (Dasgupta et al., 2004, 2006, 2007; Kiseeva et al., 2009; Yaxley and Brey, 2004). That melt may have formed out of eclogite in a plume with a potential temperature of ~1650 °C at a depth of 300–250 km, or 30–40 km deeper than in the ambient peridotite (Dasgupta et al., 2007). This is approximately the depth of the lithospheric root (“keel”) of the Siberian craton beneath the Maimecha–Kotui province (Artemieva and Mooney, 2001). Having formed in a hot plume, the eclogitic carbonate-silicate liquid interacted with the relatively cold lithospheric base, whereby it crystallized and became entrapped in the latter to cause enrichment of lithospheric peridotite with incompatible elements, including carbon dioxide and water. The eclogite component may be responsible also for the slightly higher oxidation of peridotite. Simulation of melting and metasomatism (Fig. 18, *b*) using the procedure from (Sobolev et al., 2000, 2005a), with the model parameters as in Table 6, provided a satisfactory fit (within a relative error of 20%) to all measured trace-element abundances, except Sr, at 5% partial melting of eclogite at the first stage (producing carbonate-silicate liquid), its 10% addition to

peridotite at the second stage (metasomatism), and subsequent 11% melting of metasomatized peridotite. Unlike the single-stage model of peridotite melting (Fig. 18, *a*), the three-stage scenario is quite well consistent with high Ti and Eu in meimechites. The only exception is Sr which may be overestimated in the model (Fig. 18, *b*) for the great depth of the carbonate-silicate melt generation due to its possible equilibrium with Sr-rich Ca perovskite in eclogite. Indeed, as Walter et al. (2008) showed, carbonate-silicate melt derived from eclogite at depths below 300 km has prominent Sr depletion. Thus, a single petrogenetic model for both meimechites and Gudchikhinskaya suite flood basalts can reproduce the trace-element signatures of meimechite primary magma.

Transport of meimechite magma that was generated at depths below 200 km was possible only along fractures in the very thick lithosphere of the area (Artemieva and Mooney, 2001).

The three-stage model provides good account for the succession of the meimechite and picrite sources. The Gudchikhinskaya suite picrites were produced by a reaction of high-degree eclogite melt with mantle peridotite and subsequent large-scale melting at depths of 180–130 km (Sobolev et al., 2009a). Their composition is reproduced in the same model as that of meimechites but with higher degrees of eclogite melting, formation of reaction pyroxenite, and its ensuing high-degree partial melting (Fig. 18, Table 6).

Finally, the suggested model can explain the initial sulfide depletion in the peridotite source if the latter is assumed to be depleted harzburgite of the craton root. The meimechite source have $^{187}\text{Os}/^{188}\text{Os}$ ratios in a range of 0.1232–0.1247 (Carlson et al., 2006), which are much higher than one may expect for a harzburgite source depleted in the course of Archean melting. Therefore, notable input of Re and radiogenic Os must have been associated with metasomatism, possibly, repeated one.

Origin of dunites in Guli complex. Dunites in the Guli complex (borehole G-1) occur in association with meimechites. The compositions of dunites bear signature of their genetic relation with meimechites, namely:

- most major-element abundances correspond to the trend of olivine accumulation in meimechite magma (Fig. 3);
- patterns of incompatible trace elements mimic the spectra of meimechites at the lower level of concentrations (Fig. 4);
- grain cores in olivines from dunite G-1-22 are compositionally similar to those of meimechite olivines (Figs. 5, 6; Table 2);
- dunite and meimechite olivines are generally equally enriched in Fo, Ti, Mn, and Ca.

Taking into account the composition of the alkalic melt entrapped in dunite olivines (Sobolev and Slutski, 1984), one may infer that dunites possibly were olivine cumulates of meimechite magma, as it was hypothesized in (Vasiliev and Zolotukhin, 1975).

The unusual zoning of olivines from the dunite sample G-1-22 (Fig. 6, *d*) may result from Ca and Cr diffusion from olivine into interstitial clinopyroxene during temperature drop in the subsolidus conditions. The process was likely quite rapid

and spared the cores of large olivine grains. The characteristic sizes of the uniform domain in the rims of olivine grains and in small crystals (50–30 μm) have implications for the crystallization time of the specific dunite body sampled at a depth of 310 m in G-1: This time is less than a few months, as calculated with the diffusion coefficients of Ca in magnesian olivine in oxidizing conditions (Jurewicz and Watson, 1988), at 1100 °C (Sobolev and Slutski, 1984). Therefore, it must have been a small and shallow body.

This inference of dunite origin is hard to contest for the analyzed samples, but its extrapolation to all Guli dunites has to allow for alternative opinions as well (Landa and Lyapunov, 1984; Malitch, 1995) and is worth of special study.

A thermomechanical model

The above petrological-geochemical model provides constraints for the thermomechanical model of meimechite magmatism. Below we summarize major constraints and then present the problem formulation, the solution technique, and modeling results.

Major constraints for a thermomechanical model. A successful model of the meimechite magmatism must fit the following constraints. (I) Characteristic time and spatial scales for the Siberian Trap Province are 1–2 Myr and 1000–2000 km, respectively. (II) The potential temperature of the meimechite magmas source was similar to 1640 °C at a pressure of 6 GPa, respectively. (III) Source of the meimechite magmas was depleted peridotite that was metasomatized by the carbonate-silicate melts. (IV) Meimechite magmas are known only at the margin of the Siberian Trap Province, where the lithosphere of the shield becomes thicker than some 200 km.

Problem formulation and modeling procedure. The general problem includes two parts: (1) temperature pattern in the lithosphere near the shield edge by the time of plume rise and (2) lithospheric temperature evolution associated with plume-lithosphere interaction.

1. The formulation of problem 1 may be as follows. In a model domain of 1200 km wide and 650 km deep, consider an initial 2D temperature distribution (Fig. 19, *a*) in a lithosphere of variable thickness (from 150 km on the platform to 250 km on the nearby shield) consisted from crust and mantle lithosphere, which is composed of peridotite depleted by high-degree partial melting and has a low density (Jordan, 1975, 1978; Sobolev and Sobolev, 1977) and a high viscosity (Hirth and Kohlstedt, 1996). Hereafter, we extract adiabatic gradient from temperature and consider potential temperature instead of ambient temperature. Potential temperature is equal to 0 °C at the surface and 1350 °C at the bottom of the model domain. At the side boundaries of the model domain the heat flow is set to 0. At the starting time, the lithospheric potential temperature is steady-state and changes from 0 °C at the surface to 1350 °C at the prescribed lithosphere–asthenosphere boundary (Fig. 19, *a*). This simplified temperature pattern is obviously unlikely. A more realistic temperature pattern at the

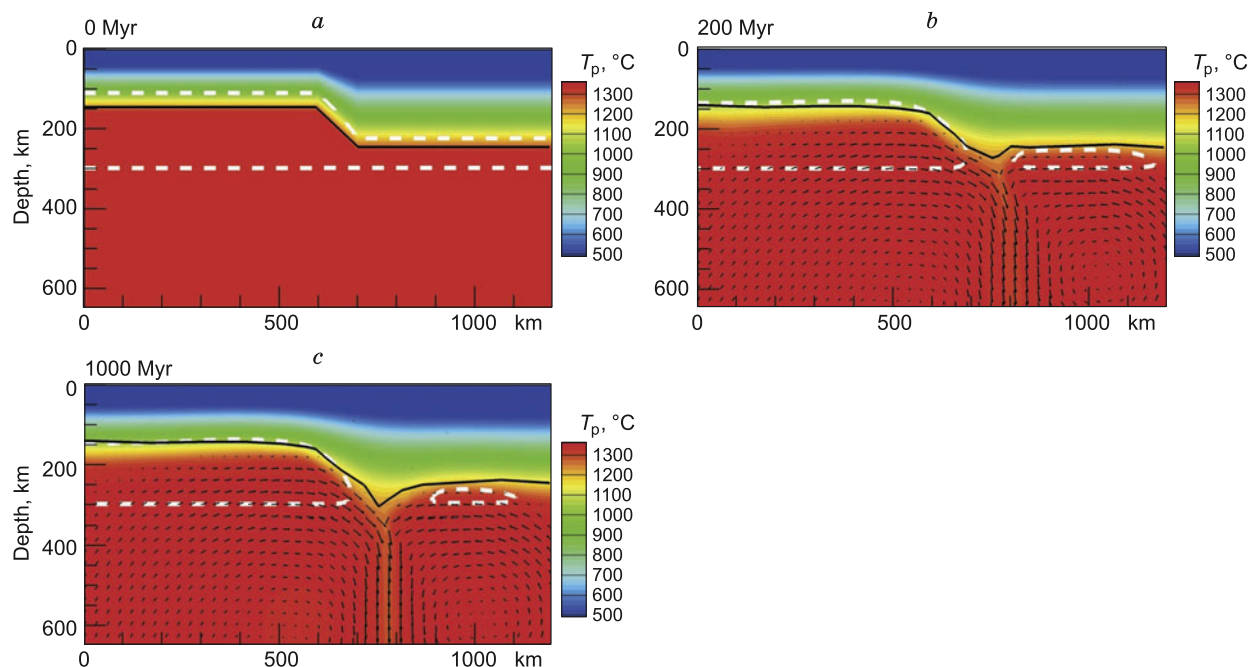


Fig. 19. Temperature evolution in the model of the cooling shield margin. Potential temperature (T_p) pattern is color-coded and arrows are velocity vectors. White dashed line bounds stability field of carbonatite melt in peridotite (Dasgupta et al., 2007), which in depleted lithosphere thicker than 180 km almost disappears after 200 Myr of cooling. Due to the edge convection, cooling of the lithosphere is slowing down with time and almost stops after 200–300 Myr. *a–c* are explained in text.

time of plume rise can be estimated by modeling the evolution of the simplified distribution through time over a few hundreds of Myr. It is assumed that in the course of its evolution the lithosphere moves at a constant velocity (2 cm/yr, in the direction perpendicular to the plain of Fig. 19), and all model boundaries are open to free flow of material.

2. The solution of the first problem is used as the starting model for the problem of plume-lithosphere interaction. Similar to the previous studies (Burov and Guillou-Frottier, 2005; Manglik and Christensen, 2006), the plume head is simulated by an elevated temperature in the domain with large radius (here 400 km, see Fig. 20, *a*) and plume conduit by an elevated temperature in the 100 km wide zone at the bottom of the model domain. The position of the plume axis with respect to the shield/platform boundary, as well as the plume temperature, are the model parameters, which are defined in order to fit observations. The mechanic and thermal boundary conditions outside the plume are the same as in problem 1. In accord with the petrological model, we assume that plume contains high amount of recycled material (15% of eclogite). Using modeling technique by Sobolev and Babeyko (1994), we estimate that for the content of recycled component of 15% the density of the plume material is by about 20 kg/m³ higher than density of the asthenosphere at the same temperature and pressure.

Solving both problems requires numerical techniques that can allow for a realistic nonlinear rheology of rocks in a broad range of temperatures (0–1700 °C), pressures (0–7 GPa), and deviatoric stresses (0–500 MPa) to fit the conditions of interaction between a plume and a thick lithosphere of a Precambrian shield. In this study we apply a finite-element

technique of numerical solution of conservation equations for momentum, mass, and energy based on the dynamic relaxation algorithm FLAC adopted for the geodynamic applications by Polyakov et al. (1993). The original 2D (plus time) code is complemented with a technique for transfer of material state variables (including stress tensor) with markers that track material properties (Babeyko et al., 2002; Sobolev and Babeyko, 2005) and is extended to the case of 3D (plus time) processes (Sobolev et al., 2005b; Petrunin and Sobolev, 2006, 2008). The assumed rheology is nonlinear and visco-elasto-plastic with parameters determined through laboratory tests. This numerical method was successfully used to model the thermomechanical processes associated with orogeny in the Andes (Babeyko and Sobolev, 2005; Sobolev and Babeyko, 2005), with deformation at the Dead Sea transform fault (Sobolev et al., 2005b), and with formation of pull-apart basins (Petrunin and Sobolev, 2006, 2008). The version applied in this study allows simulating motion in three dimensions but assumes that all variables depend only on two space coordinates and on time. For details see (Sobolev, et al., 2005b). Model parameters are listed in Table 7.

Modeling results. Cooling of the lithosphere near the shield edge (Fig. 19, *a–c*) is attendant with mantle convection, previously reported by King and Anderson (1998). The boundary of the depleted lithosphere slightly changes in time as a result of deformation, but more important is that cooled asthenospheric material is added to depleted lithosphere through time. Thus, the mechanic lithosphere (a zone of cold high-viscosity mantle) extends at the account of nondepleted peridotite. However, the edge convection slows down cooling of the lithosphere. Consequently, the thickness of the peridotite-

Table 7. Parameters of the thermomechanical model

Parameter	Upper crust	Lower crust	Depleted mantle	Asthenosphere/plume
Density at 0 °C and 0 GPa (kg/m ³)	2700	2900	3260	3300/3320
Thermal expansion coefficient (1/K)	3.7	2.7	3.0	3.0
Elastic moduli, K; G (GPa)	55; 36	63; 40	122; 74	122; 74
Heat capacity (J/kg/K)	1200	1200	1200	1200
Thermal conductivity (W/K/m)	2.0	2.5	3.3	3.3
Heat generation (μW/m ³)	1.5	0.2	0	0
Friction coefficient	0.5	0.5	0.5	0.5
Pre-exponential factor for dislocation creep log(Bn), (Pa ⁻ⁿ s ⁻¹)	-28.0 ⁽¹⁾	-15.4 ⁽²⁾	-15.2 ⁽³⁾	-14.7 ⁽³⁾
Stress exponent, <i>n</i>	4.0 ⁽¹⁾	3.0 ⁽²⁾	3.5 ⁽³⁾	3.5 ⁽³⁾
Activation Energy and Volume for dislocation creep, (kJ/mol, cm ³)	223 ⁽¹⁾	356 ⁽²⁾	530 ⁽³⁾	480 ⁽³⁾
	15	15	17	12

⁽¹⁾ quartz (Gleason and Tullis, 1995); ⁽²⁾ anorthite (Rybacki and Dresen, 2000); ⁽³⁾ olivine (Hirth and Kohlstedt, 2003), dry for depleted mantle and with water content of 1000 H/10⁶Si for the asthenosphere and plume.

tic layer that is added to the lithosphere, does not change much after 200–300 Myr of cooling, staying below 30 km. The white dashed line in Fig. 19 bounds the stability field of carbonate melt in peridotite according to (Dasgupta et al., 2007). The stability field of carbonatite melt in depleted lithosphere reduces with time and almost disappears after 200 Myr of cooling in the lithosphere thicker than 180 km. This means that intense metasomatism of thick depleted shield lithosphere is unlikely without a hot plume.

The solution to problem 1 for a cooling time of 200 Myr (Fig. 19, *b*) was used as a starting model to simulate plume-lithosphere interaction. The model of Fig. 20 (color coded is the mantle temperature pattern 0.5 and 2.5 Myr after intrusion of a plume with a potential temperature of 1650 °C) predicts that plume material spreads along the bottom of the lithosphere with the speed of more than 2000 km/Myr. Simultaneously, the plume erodes most of the lowermost lithospheric layer composed from a nondepleted peridotite thus exposing the depleted lithosphere for heating. Consequently, carbonatite melt becomes stable in the depleted shield lithosphere to create conditions for intense metasomatism of the lithospheric base. One has to bear in mind that infiltration of carbonatite melt into the depleted shield lithosphere can be very slow being controlled by viscosity of solid matrix (Connolly and Podladchikov, 2000) which is high because of depletion-related dehydration (Hirth and Kohlstedt, 1996). As a result, one may expect that metasomatism by plume-associated carbonatite melt is restricted to the zone near the base of the depleted lithosphere, but is very intense. When accumulated, this melt can erupt in kimberlite volcanism under certain mechanic conditions (Artyushkov and Sobolev, 1977).

Application of our model to the meimechite magmatism in details is discussed in the next section. Here we check how our model fits the above-mentioned major model constraints.

Very high speed of the spreading of the plume below the shield lithosphere in the model agrees well with temporal and spatial scales of Siberian Traps (1–2 Myr, 2000 km), thus

fitting model constraint I. This result is not obvious, because our model plume contains high amount (15%) of dense recycled material that reduces plume buoyancy by 3 times compared to the “classical” plume of the same temperature.

Another important point is that according to our model the potential temperature in the plume must have been not lower than 1650 °C. Otherwise the PT conditions for the meimechite melts (model constraint II) can not be fulfilled.

Although the bottom of depleted lithosphere is significantly heated by the plume, its temperature does not exceed 1400 °C, even if the plume potential temperature is as high as 1650 °C (Fig. 20). That happens because the thermal boundary layer between the relatively cold depleted lithosphere and the hot internal part of the plume does not allow heating the depleted lithosphere up to the plume temperature even during 10 Myr. The consequence is that our numerical model is apparently inconsistent with the model constraint III that the source of the meimechite melts was metasomatized depleted peridotite. The way out of this problem as well as the consistency of our model with the model constraint IV is discussed below.

A model of meimechite origin

Estimates of very high temperatures and unusual composition (containing recycled material) of deep sources for early flood basalts (Gudchikhinskaya suite of Norilsk region, Sobolev et al., 2009a) as well as especially high temperatures for the source of the meimechites, strongly suggest hot mantle plume as a source of heat and material for Siberian Trap Province. Moreover, our numerical model (Fig. 20) confirms that the speed of spreading of the mantle plume containing large amount of recycled crust beneath lithosphere is consistent with the temporal and spatial scales of Siberian Traps.

Figure 21 presents the petrogenetic model of meimechites based on the reported analytical data and numerical experiments. We suggest that recycled Precambrian oceanic crust,

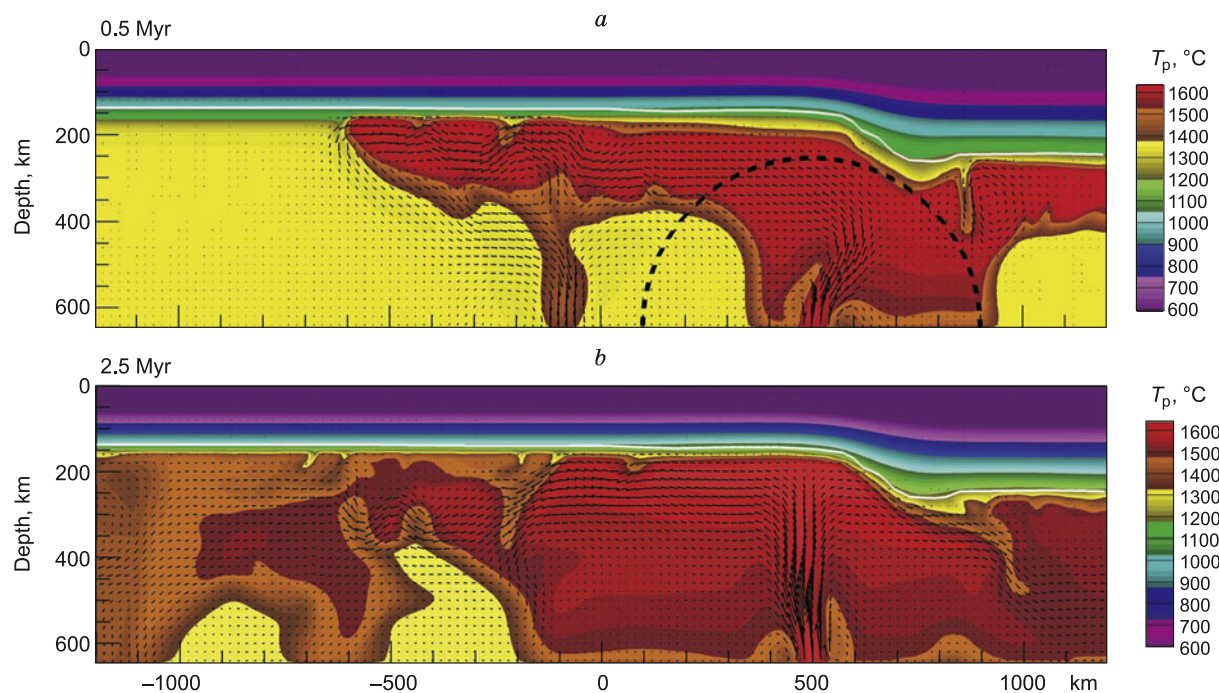


Fig. 20. Mantle temperature evolution due to the plume-lithosphere interaction. Potential temperature (T_p) pattern is color-coded and arrows are velocity vectors. White solid line bounds depleted mantle. *a*, 0.5 Myr after plume injection, dashed half-circle shows plume head at time 0. *b*, 2.5 Myr after plume injection. Plume material spreads below the lithosphere with the speed of more than 2000 km/Myr and erodes most of the lower nondepleted part of the lithosphere.

in the form of SiO₂ oversaturated carbonated eclogite, was entrained within a mantle plume with potential temperature of at least 1650 °C. At depths between 400–300 km, melting was restricted to generation of purely carbonate partial melts of very low degrees (fractions of percent) which played only a minor role in redistribution of trace elements. At depth of around 250–300 km, eclogite experienced higher-degree partial melting (e.g., up to 5%) to form carbonate-silicate liquid which became focused in porous magma conduits moving through ambient peridotite (Batanova and Savelieva, 2009; Lambart et al., 2009) towards the deep roots of the Siberian craton. Carbonate-silicate melt may have accumulated and stored in these roots thereby metasomatising and partly oxidizing the “dry” and originally cold depleted garnet harzburgite lithosphere (Griffin et al., 2009; Sobolev, 1974). Harzburgite experienced rather high-degree partial melting in Archean time and, for that reason, was free from sulfide phase and notably dehydrated.

At depths shallower than 200 km, recycled eclogite in the plume further melted producing high Si melts which reacted with peridotite forming hybrid pyroxenite (e.g., Sobolev et al., 2007). This rock started melting at depth of around 170 km (Fig. 21) producing large amount of magmas which triggered thermochemical erosion or delamination of lithosphere and initiated formation of major type of Siberian flood basalts by decompression melting of peridotite (Sobolev et al., 2009a). Mechanism of such thermochemical erosion or delamination is not clear at a moment. Our model (Fig. 20) demonstrates that the thermomechanical process alone do not lead to erosion of the depleted shield lithosphere, even if realistic, strongly

nonlinear rheology of the rocks is considered. Additional processes like intrusion of magmas into the lithosphere leading to the Rayleigh–Taylor instability (Elkins-Tanton and Hager, 2000) should be likely invoked.

Delaminated lithosphere that included fragments of locally metasomatized depleted harzburgite subsided into the plume and was heated. Heating of metasomatized zones in harzburgite caused their melting, but host dehydrated harzburgite, due to its high viscosity resulting from dehydration of olivine (Hirth and Kohlstedt, 1996), was able to maintain low-degree partial melts. Further heating of the blocks of metasomatized harzburgite generated relatively high-degree magnesian ultramafic partial melt rich in incompatible elements, including carbon dioxide and water. The rather short time scale of the process (less than 1 Myr) constrains the size of these fragments to be less than 10 km. Subsiding blocks of the delaminated depleted lithosphere of that size were able to heat-up to the temperatures of the hottest interior parts of the plume in accordance with the estimated temperatures for the sources of meimechites (see domain bounded by the solid white line in Fig. 21) and thus fulfilling model constraint III. When produced under major melting zone of pyroxenites, these melts mixed up with much more voluminous basalts and therefore did not show up on the surface. However, when metasomatized harzburgite blocks followed convection path within the plume on the right side of the plume axis (arrows in Fig. 21) they were accumulated under thicker part of the lithosphere aside from major melting zone above (Fig. 21). In this case partial melts from such blocks (primary meimechite) did not mix with basalts and therefore could be recognized at the

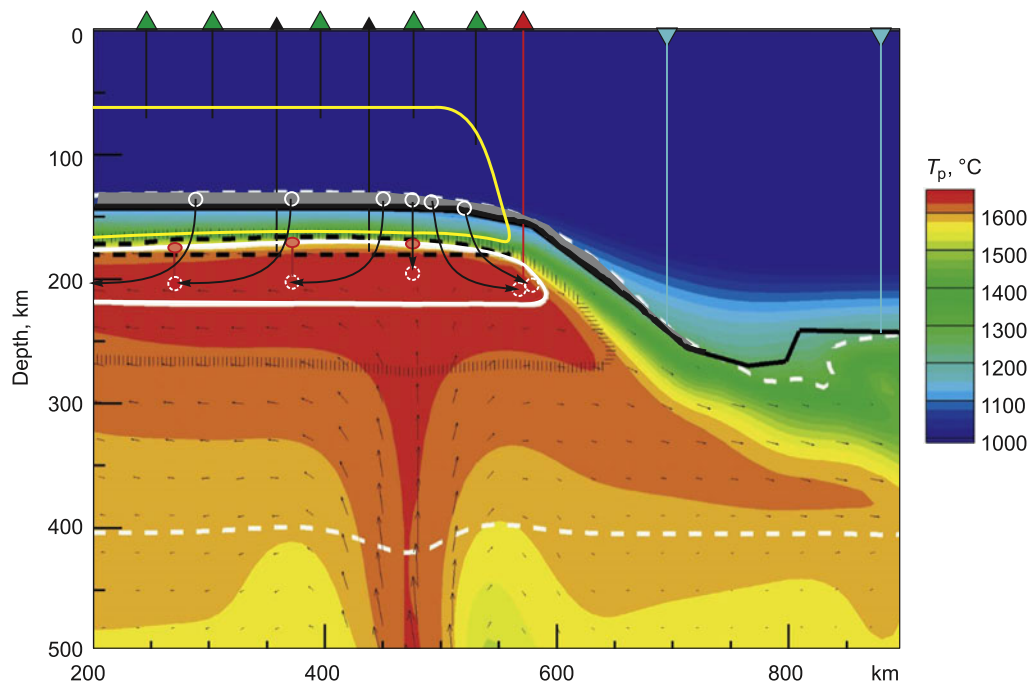


Fig. 21. A generalized model for the origin of Siberian meimechites, flood basalts and kimberlites. Background is the potential temperature (T_p , °C) distribution resulted from the interaction of plume and shield lithosphere 2.5 Myr after plume injection (zoom in of Fig. 20, *b*). Temperature pattern is color-coded and small arrows are velocity vectors. Black solid line marks bottom of the depleted shield lithosphere. White dashed line bounds stability field of carbonatite melt in peridotite (Dasgupta et al., 2007). Grey domain is the metasomatized depleted mantle. Black shaded curve bounds field of carbonate-silicate melting for eclogite (Dasgupta et al., 2007) and black dashed curve bounds “dry” pyroxenite solidus (Sobolev et al., 2007). White solid curve bounds stability field of meimechite primary melt (Table 6). Yellow curve indicates the volume of delaminated lithosphere required to produce major magmatic event of Siberian flood basalts (Sobolev et al., 2009a). Solid black arrows and gray-red circles with dashed white outline point out the subsidence direction and heating of blocks of delaminated metasomatized depleted mantle. Color-coded triangles at the surface and connected lines indicate magmas and depth of their sources: black, early type of Siberian flood basalts (Gudchikhinskaya suite of Norilsk region) formed from pure pyroxenitic source (Sobolev et al., 2009a); green, major type of Siberian flood basalts formed from mixed peridotite-pyroxenite source (Sobolev et al., 2009a); red, meimechites; blue, kimberlites. Red ellipses indicate primary meimechite melts that are mixed up with more voluminous pyroxenite-derived melts and thus are indistinguishable at the surface. Note that “dry” peridotite would start melting only after lithosphere delamination.

surface. This explains why meimechite magmas are known only at the margin of the Siberian Trap Province thus fulfilling model constraint IV.

Meimechite magma rapidly rose along fractures through cold lithosphere being subject to degassing and attendant further oxidation (Mathez, 1984). At shallow depths, it crystallized and intruded or erupted thus forming olivine porphyritic meimechites and dunites, their olivine cumulates. Fractional crystallization of meimechites, together with crust assimilation, gave rise to the alkaline series of the Maimecha–Kotui igneous province (Kogarko and Ryabchikov, 2000; Sobolev et al., 1991).

Kogarko and Ryabchikov (2000) suggested a somewhat similar multi-stage model for origin of meimechite but with a metasomatic agent of a different source (depleted mantle instead of recycled oceanic crust) and of different composition (silicate rather than silicate-carbonate melt). In addition, they suggest that melting took part in-situ in the metasomatized root of Siberian craton rather than in its delaminated fragments as in our model. We think our model is better suited to geochemical and thermomechanical constraints presented above. In particular, it better explains geochemical similarity between meimechites and flood basalts and resolves problem

in reaching exceptionally high temperatures by heating of craton root (see previous section and Fig. 21).

Unlike meimechites, primary magmas of the Gudchikha flood volcanics, and, possibly, also of tholeiites which coexist with alkali lavas in the Maimecha–Kotui province (Arndt et al., 1998; Vasiliev and Zolotukhin, 1975), originated at much shallower depths in zones of lithospheric thinning by melting of reaction pyroxenite (Fig. 21). Their generation predated the formation of meimechite magma in the Maimecha–Kotui province (Fedorenko and Czamanske, 1997) because delamination and heating of the fragments of lithospheric root (source of meimechites) to the onset of melting apparently took some time.

As it is shown before (Fig 19), the metasomatism of thick lithospheric root by carbonatite melt is unlikely by free mantle convection alone, without hot plume. This result is also essential for origin of kimberlites, which show considerable compositional similarity to meimechite and closely associate with them in space and time (Carlson et al., 2002). Carbonatite melt of recycled oceanic crust (eclogite) was likewise invoked before as a source of C, Cl, and incompatible elements in kimberlite magma (Kamenetsky et al., 2008). The latter model differs from ours primarily in melting temperature. One may

presume that kimberlite, with a proximal composition of the metasomatized source, can melt at lower temperatures at the root of craton just moderately heated by the plume (Fig. 21). Then its composition is defined by lower-degree partial melting and higher content of CO₂ or, maybe, also of Cl (Kamenetsky et al., 2004). Correspondingly, kimberlite magma must be much less voluminous than meimechite magma.

Conclusions

We analyzed the least altered meimechite and dunite samples from boreholes G-1 and G-3 within the Guli complex in the Maimecha–Kotui igneous province of the northern Siberian craton and used the analytical data on olivine phenocrysts and melt inclusions in them to model the crystallization and melting paths and to infer the origin of meimechites. We also computed thermomechanical model of interaction of a hot mantle plume with the shield lithosphere of variable thickness, using realistic temperature and stress dependent visco-elasto-plastic rocks rheology and advanced finite element solution technique. Specifically, our conclusions are as follows.

1. The meimechite composition is remarkable by simultaneous enrichment in incompatible lithophile elements, MgO, Ni, and Ca and depletion in Si and in elements compatible with garnet, such as HREE, Y, Sc, and Al. Dunites mimic the meimechite spectra in detail but at lower concentration levels.

2. Olivines from meimechites have high and variable Mg# (Fo = 93–86) and Ca, Mn, and Ti concentrations considerably above the respective abundances in olivines of similar Mg# from most of known mantle magmas; Cr and Ni are, on the contrary, lower than in the greatest number of magnesian olivines from within-plate magmas and komatiites. The Mn/Fe and Ni/MgO ratios in olivine from meimechites correspond to a peridotite mantle source.

3. The primary composition of melt entrapped in olivine from meimechites records fractional crystallization of olivine, at temperatures between 1540 and 1420 °C, from an alkaline ultramafic melt with MgO from 22 to 15 wt.%, and at oxygen fugacity one or two orders of magnitude above the QFM buffer. Meimechite primary magma was inferred to contain more than 1 wt.% H₂O and be undersaturated with sulfide liquid. S and Cl in it were in a positive correlation and both behaved as incompatible elements. High contents of K and Na in olivine-trapped melt indicate regular loss of alkalis (especially Na) from rocks at the late magmatic or post-magmatic stages.

4. At shallow depth parental magma of meimechites contained about 24% MgO and was largely degassed. Its trace-element abundances correspond to significant amount of garnet, K clinopyroxene, and, possibly, Ca perovskite in the mantle source and are similar to the respective patterns for the Gudchikhinskaya suite picrites (Norilsk area), which mark the onset of the major flood basaltic event in the Siberian craton.

5. Meimechite primary magma was initially high in CO₂ (5.8 wt.%) and H₂O (1.8 wt.%) and resulted from partial melting of peridotite at 200–270 km and at a potential temperature of near 1640 °C. The oxygen fugacity of the peridotite source was at the QFM buffer.

6. The analyzed dunite samples from the Guli complex have chemistry and mineralogy indicating their close relation to meimechites and could possibly originate by olivine cumulation in meimechite like melt.

7. Estimates of very high temperatures and unusual composition (containing recycled material) of deep sources for early flood basalts (Gudchikhinskaya suite of Norilsk region) as well as especially high temperatures for the source of the meimechites, strongly suggest hot mantle plume as a source of heat and material for Siberian Trap Province. Moreover, the numerical model confirms that the speed of spreading of the mantle plume containing large amount of recycled crust beneath lithosphere is consistent with the temporal and spatial scales of Siberian Traps.

8. Generation of primary magmas of the Gudchikhinskaya suite picrites and the Maimecha–Kotui meimechites which represent, respectively, the beginning and the end of Siberian flood magmatism, can be explained by a single model that is consistent with both petrological-geochemical and thermomechanical conclusions of this study. According to this model, a Permian-Triassic plume, with potential temperature of about 1650 °C, transported a large amount of recycled Precambrian oceanic crust (up to 15%) as SiO₂-oversaturated carbonated eclogite. Low-degree partial melting of eclogite at depths of 250–300 km produced carbonate-silicate melt that metasomatized the lithospheric roots of the Siberian shield. Further rise of the plume in zones of relatively attenuated lithosphere (Norilsk area) led to progressive melting of eclogite and formation of reaction pyroxenite, which then melted at depths of 140–180 km. Thus, a large volume of melt (Gudchikhinskaya suite) penetrated into the lithosphere and caused its destabilization and delamination. As a result, the plume material rose to depths less than 60 km and underwent decompression melting producing main volume of Siberian flood basalts. Delaminated lithosphere that included fragments of locally metasomatized depleted harzburgite subsided into the plume and was heated to the temperatures of the plume interior with subsequent generation of meimechite magma. When produced under major melting zone of pyroxenites, meimechite melts mixed up with much more voluminous basalts and therefore did not show up on the surface. However, some of the metasomatized harzburgite blocks following convection path within the plume were accumulated under thicker part of the lithosphere aside from major melting zone above. In this case meimechites did not mix with basalts and therefore could be recognized at the surface in the Maimecha–Kotui igneous province.

9. The thermomechanical model also suggests that intense metasomatism of this lithosphere is unlikely without a hot plume. Metasomatism of the shield's highly viscous dehydrated and depleted lithosphere with plume-associated carbonatite melt appears to be restricted to a zone near the

lithospheric base but must be very intense. Contrary to meimechites melting of these metasomatized zones in situ may produce protokimberlite melts without significant heating.

10. We suggest that meimechites, uncontaminated Siberian flood basalts and kimberlites all shear the same source of strongly incompatible elements, the carbonated recycled oceanic crust carried up by hot mantle plume.

Acknowledgements. We appreciate discussions with A.W. Hofmann, R. Dasgupta, N. Arndt, Yu.R. Vasiliev, A.A. Kadik, G.G. Lopatin, and O.I. Lukanin and constructive criticism by V.S. Kamenetsky and two reviewers. Heating and quenching of melt inclusions in olivines was carried out at Vernadsky Institute of Geochemistry and Analytical Chemistry, Moscow (laboratory of A.A. Kadik) by M.V. Volovetsky. Trace elements were determined by LA-ICPMS, at the Max Planck Institute for Chemistry (laboratory of K.P. Jochum) with assistance of B. Stoll.

The study was supported by Russian Foundation for Basic Research (grants 09-05-01193-a and 09-05-01242-a) and by the President of the Russian Federation (grant NSh-150.2008.5), and was carried out as part of Basic Research Program 8 of the Earth Science Department of the Russian Academy of Sciences.

References

- Allégre, C. J., Turcotte, D. L., 1986. Implications of a two-component marble-cake mantle. *Nature* 323, 123–127.
- Arndt, N., Lehnert, K., Vasilev, Y., 1995. Meimechites–highly magnesian lithosphere-contaminated alkaline magmas from deep subcontinental mantle. *Lithos* 34 (1–3), 41–59.
- Arndt, N., Chauvel, C., Czamanske, G., Fedorenko, V., 1998. Two mantle sources, two plumbing systems: tholeiitic and alkaline magmatism of the Maymecha River basin, Siberian flood volcanic province. *Contrib. Mineral. Petrol.* 133 (3), 297–313.
- Artemieva, I.M., Mooney, W.D., 2001. Thermal thickness and evolution of Precambrian lithosphere: A global study. *J. Geophys. Res.* 106, 16,387–16,414.
- Artyushkov, E.V., Sobolev, S.V., 1977. The mechanism of the rise of kimberlite magma from mantle depths. *Dokl. Akad. Nauk SSSR* 236 (3), 692–695.
- Babeyko, A.Y., Sobolev, S.V., 2005. Quantifying different modes of the late Cenozoic shortening in the Central Andes. *Geology* 33 (8), 621–624.
- Babeyko, A.Y., Sobolev, S.V., Trumbull, R.B., Oncken, O., Lavier, L.L., 2002. Numerical models of crustal scale convection and partial melting beneath the Altiplano-Puna plateau. *Earth Planet. Sci. Lett.* 199, 373–388.
- Basu, A.R., Poreda, R.J., Renne, R., Teichmann, F., Vasiliev, Y.R., Sobolev, N.V., Turrin, B.D., 1995. High-He-3 plume origin and temporal-spatial evolution of the Siberian flood basalts. *Science* 269, 822–825.
- Batanova, V.G., Savelieva, G.N., 2009. Migration of melts in the mantle beneath spreading zones and formation of replacement dunites: problem overview. *Russian Geology and Geophysics (Geologiya i Geofizika)* 50 (9), 763–778 (992–1012).
- Borisov, A.A., Shapkin, A.I., 1989. A new empirical equation relating Fe^{3+}/Fe^{2+} in natural melts with their chemistry, oxygen fugacity, and temperature. *Geokhimiya*, No. 6, 892–897.
- Burov, E., Guillou-Frottier, L., 2005. The plume head-continental lithosphere interaction using a tectonically realistic formulation for the lithosphere. *Geophys. J. Int.* 161, 469–490.
- Campbell, I.H., Griffiths, R.W., 1992. The changing nature of mantle hotspots through time—implications for the chemical evolution of the mantle. *J. Geol.* 100 (5), 497–523.
- Carlson, R.W., Czamanske, G., Fedorenko, V., Ilupin, I., 2006. A comparison of Siberian meimechites and kimberlites: Implications for the source of high-Mg alkaline magmas and flood basalts. *Geochem. Geophys. Geosys.* 7, Q11014, doi:10.1029/2006GC001342.
- Cartigny, V., Pineau, F., Aubaud, C., Javoy, M., 2008. Towards a consistent mantle carbon flux estimate: Insights from volatile systematics (H_2O/Ce , δD , CO_2/Nb) in the North Atlantic mantle (14 degrees N and 34 degrees N). *Earth Planet. Sci. Lett.* 265 (3–4), 672–685.
- Connolly, J.A.D., Podladchikov, Yu.Yu., 2000. Temperature-dependent viscoelastic compaction and compartmentalization in sedimentary basins. *Tectonophysics* 324 (3), 137–168.
- Cordery, M.J., Davies, G.F., Campbell, I.H., 1997. Genesis of flood basalts from eclogite-bearing mantle plumes. *J. Geophys. Res.* 102 (B9), 20,179–20,197.
- Dalrymple, G.B., Czamanske, G.K., Fedorenko, V.A., Simonov, O.N., Lanphere, M.A., Likhachev, A.P., 1995. A reconnaissance Ar-40/Ar-39 geochronological study of ore-bearing and related rocks, Siberian Russia. *Geochim. Cosmochim. Acta* 59, 2071–2083.
- Danyushevsky, L.V., 2001. The effect of small amounts of H_2O crystallization of mid-ocean ridge and backarc basin magmas. *J. Volc. Geotherm. Res.* 110 (3–4), 265–280.
- Danyushevsky, L.V., Sobolev, A.V., 1996. Ferric-ferrous ratio and oxygen fugacity calculations for primitive mantle-derived melts: Calibration of an empirical technique. *Miner. Petrol.* 57 (3–4), 229–241.
- Danyushevsky, L.V., Della-Pasqua, F.N., Sokolov, S., 2000. Re-equilibration of melt inclusions trapped by magnesian olivine phenocrysts from subduction-related magmas: petrological implications. *Contrib. Mineral. Petrol.* 138 (1), 68–83.
- Danyushevsky, L.V., McNeill, A.W., Sobolev, A.V., 2002. Experimental and petrological studies of melt inclusions in phenocrysts from mantle-derived magmas: an overview of techniques, advantages and complications. *Chem. Geol.* 183 (1–4), 5–24.
- Dasgupta, R., Hirschmann, M.M., Withers, A.C., 2004. Deep global cycling of carbon constrained by the solidus of anhydrous, carbonated eclogite under upper mantle conditions. *Earth Planet. Sci. Lett.* 227, 73–85, doi:10.1016/j.epsl.2004.08.004.
- Dasgupta, R., Hirschmann, M.M., Stalker, K., 2006. Immiscible transition from carbonate-rich to silicate-rich melts in the 3 GPa melting interval of eclogite plus CO_2 and genesis of silica-undersaturated ocean island lavas. *J. Petrol.* 47, 647–671.
- Dasgupta, R., Hirschmann, M.M., Smith, N.D., 2007. Partial melting experiments of peridotite + CO_2 at 3 GPa and genesis of alkalic ocean island basalts. *J. Petrol.* 48 (11), 2093–2124.
- Dobretsov, N.L., 2008. Geological implications of the thermochemical plume model. *Russian Geology and Geophysics (Geologiya i Geofizika)* 49 (7), 441–454 (587–604).
- Dobretsov, N.L., Kirdyashkin, A.A., Kirdyashkin, A.G., Vernikovskiy, V.A., Gladkov, I.N., 2008. Modelling of thermochemical plumes and implications for the origin of the Siberian traps. *Lithos* 100, 66–92.
- Elkins-Tanton L.T., Hager, B.H., 2000. Melt intrusion as a trigger for lithospheric foundering and the eruption of the Siberian flood basalt. *Geophys. Res. Lett.* 27, 3937–3940.
- Elkins-Tanton, L.T., Draper, D.S., Agee, C.B., Jewell, J., Thorpe, A., Hess, C., 2007. The last lavas erupted during the main phase of the Siberian flood volcanic province: results from experimental petrology. *Contrib. Mineral. Petrol.* 153, 191–209.
- Falloon, T.J., Danyushevsky, L.V., 2000. Melting of refractory mantle at 1.5, 2.0 and 2.5 GPa under anhydrous and H_2O -undersaturated conditions: Implications for the petrogenesis of high-Ca boninites and the influence of subduction components on mantle melting. *J. Petrol.* 41 (2), 257–283.
- Falloon, T.J., Danyushevsky, L.V., Ariskin, A., Green, D.H., Ford, C.E., 2007. The application of olivine geothermometry to infer crystallization temperatures of parental liquids: Implications for the temperature of MORB magmas. *Chem. Geol.* 241 (3–4), 207–233.
- Fedorenko, V.A., Czamanske, G.K., 1997. Results of new field and geochemical studies of the volcanic and intrusive rocks of the Maymecha-Kotuy area, Siberian flood-basalt province, Russia. *Intern. Geol. Rev.* 39, 479–531.

- Fedorenko, V.A., Lightfoot, C., Naldrett, A.J., Czamanske, G., Hawkesworth, C., Wooden, J., Ebel, D., 1996. Petrogenesis of the Siberian flood-basalt sequence at Noril'sk, north central Siberia. *Intern. Geol. Rev.* 38, 99–135.
- Ford, C.E., Russel, D.G., Craven, J.A., Fisk, M.R., 1983. Olivine-liquid equilibria: temperature, pressure and composition dependence of crystal/liquid cation partition coefficients for Mg, Fe²⁺, Ca and Mn. *J. Petrol.* 24, 256–265.
- Gleason, G.C., Tullis, J., 1995. A flow law for dislocation creep of quartz aggregates determined with the molten salt cell. *Tectonophysics* 247, 1–23.
- Griffin, W.L., O'Reilly, S.Y., Afonso, J.C., Begg, G.C., 2009. The composition and evolution of lithospheric mantle: a re-evaluation and its tectonic implications. *J. Petrol.* 50 (7), 1185–1204.
- Herzberg, C., Gazel, E., 2009. Petrological evidence for secular cooling in mantle plumes. *Nature* 458, 619–622.
- Herzberg, C., O'Hara, M.J., 2002. Plume-associated ultramafic magmas of Phanerozoic age. *J. Petrol.* 43 (10), 1857–1883.
- Herzberg, C., Asimow, P.D., Arndt, N., Niu, Y.L., Leshner, C.M., Fitton, J.G., Cheadle, M.J., Saunders, A.D., 2007. Temperatures in ambient mantle and plumes: Constraints from basalts, picrites, and komatiites. *Geochem. Geophys. Geosys.* 8, Q02006.
- Hirth, G., Kohlstedt, D.L., 1996. Water in the oceanic upper mantle: Implications for rheology, melt extraction and the evolution of the lithosphere. *Earth Planet. Sci. Lett.* 144, 93–108.
- Hirth, G., Kohlstedt, D., 2003. Rheology of the upper mantle and the mantle wedge: a view from the experimentalists. *Geophysical Monograph* 138, 83–105.
- Hofmann, A.W., 1988. Chemical differentiation of the Earth: the relationship between mantle, continental crust, and oceanic crust. *Earth Planet. Sci. Lett.* 90, 297–314.
- Hofmann, A.W., 2002. Sampling mantle heterogeneity through oceanic basalts: isotopes and trace elements. *Treatise on Geochemistry* 2, 61–101.
- Hofmann, A.W., White, W.M., 1982. Mantle plumes from ancient oceanic crust. *Earth Planet. Sci. Lett.* 57, 421–436.
- Jarosevich, E.J., Nelen, J.A., Norberg, J.A., 1980. Reference sample for electron microprobe analysis. *Geostandards Newsletter* 4, 43–47.
- Jochum, K.P., Dingwell, D.B., Rocholl, A., Stoll, B., Hofmann, A.W., Becker, S., Besmehn, A., Bessette, D., Dietze, H.J., Dulski, V., Erzinger, J., Hellebrand, E., Hoppe, V., Horn, I., Janssens, K., Jenner, G.A., Klein, M., McDonough, W.F., Maetz, M., Mezger, K., Munker, C., Nikogosian, I.K., Pickhardt, C., Raczek, I., Rhede, D., Seufert, H.M., Simakin, S.G., Sobolev, A.V., Spettel, B., Straub, S., Vincze, L., Wallianos, A., Weckwerth, G., Weyer, S., Wolf, D., Zimmer, M., 2000. The preparation and preliminary characterization of eight geological MPI-DING reference glasses for in-situ microanalysis. *Geostandards Newsletter* 24, 87–133.
- Jordan, T.H., 1975. The continental tectosphere. *Rev. Geophys.* 13, 1–12.
- Jordan, T.H., 1978. Composition and development of the continental tectosphere. *Nature* 274, 544–548.
- Jurewicz, A.J.G., Watson, E.B., 1988. Cations in olivine. 2. Diffusion in olivine xenocrysts, with applications to petrology and mineral physics. *Contrib. Mineral. Petrol.* 99 (2), 186–201.
- Kamenetsky, M.B., Sobolev, A.V., Kamenetsky, V.S., Maas, R., Danyushevsky, L.V., Thomas, R., Pokhilenko, N.P., Sobolev, N.V., 2004. Kimberlite melts rich in alkali chlorides and carbonates: A potent metasomatic agent in the mantle. *Geology* 32 (10), 845–848.
- Kamenetsky, V.S., Kamenetsky, M.B., Sobolev, A.V., Golovin, A.V., Demouchy, S., Faure, K., Sharygin, V.V., Kuzmin, D.V., 2008. Olivine in the Udachnaya-East kimberlite (Yakutia, Russia): Types, compositions and origins. *J. Petrol.* 49 (4), 823–839.
- Kamo, S.L., Czamanske, G.K., Amelin, Yu., Fedorenko, V.A., Davis, D.W., Trofimov, V.R., 2003. Rapid eruption of Siberian flood-volcanic rocks and evidence for coincidence with the Permian-Triassic boundary and mass extinction at 251 Ma. *Earth Planet. Sci. Lett.* 214, 75–91.
- King, S.D., Anderson, D.L., 1988. Edge-driven convection. *Earth Planet. Sci. Lett.* 160, 289–296.
- Kiseeva, E.S., Yaxley, G.M., Kamenetsky, S., 2009. Melting of carbonated eclogite at 3.5–5.5 GPa: An experimental study. *Geochim. Cosmochim. Acta* 73 (13), A663–A663.
- Kogarko, L.N., Ryabchikov, I.D., 1995. Geochemical data on conditions of meimechite-magma generation in polar Siberia. *Geochem. Int.* 33 (11), 119–130.
- Kogarko, L.N., Ryabchikov, I.D., 2000. Geochemical evidence for meimechite magma generation in the subcontinental lithosphere of Polar Siberia. *J. Asian Earth Sci.* 18, 195–203.
- Kogarko, L.N., Zartman, R.E., 2007. A Pb isotope investigation of the Guli massif, Maymecha-Kotuy alkaline-ultramafic complex, Siberian flood basalt province, Polar Siberia. *Miner. Petrol.* 89 (1–2), 113–132.
- Kogarko, L.N., Karpenko, S.F., Lyalikov, A.V., Tepteleev, M.V., 1988. Petrogenesis of meimechite magmatism: implications from isotope data. *Dokl. Akad. Nauk SSSR* 301 (4), 939–942.
- Kogarko, L.N., Karpenko, S.F., Lyalikov, A.V., 1996. Isotope heterogeneity of the sources of alkaline magmatism in Arctic Siberia: Nd isotope data. *Geokhimiya*, No. 2, 186–189.
- Lambart, S., Laporte, D., Schiano, P., 2009. An experimental study of focused magma transport and basalt-pyroxene interactions beneath mid-ocean ridges: implications for the generation of primitive MORB compositions. *Contrib. Mineral. Petrol.* 157 (4), 429–451.
- Landa, E.A., Lyapunov, S.M., 1984. Trace-element chemistry and petrogenesis of dunites of the Guli pluton. *Dokl. Akad. Nauk SSSR* 276 (1), 243–245.
- Lightfoot, C., Howkesworth, C.J., Hergt, J., Naldrett, A.J., Gorbachev, N.S., Fedorenko, V.A., Doherty, W., 1993. Remobilisation of the continental lithosphere by a mantle plume: major-, trace-element, and Sr-, Nd-, and Pb-isotopic evidence from picritic and tholeiitic lavas of the Noril'sk District, Siberian Trap, Russia. *Contrib. Mineral. Petrol.* 114, 171–188.
- Malitch, K.N., 1995. PGE patterns in ultramafics of the Guli complex: petrogenetic implications. *Zap. RMO (Russian Mineralogical Society Transactons)*, Issue 5, 16–30.
- Malitch, K.N., 1999. PGE Patterns in Clinopyroxenite-Dunite Complexes of East Siberia: Geochemistry, Mineralogy, and Petrogenesis [in Russian]. Sankt-Peterburgskaya Kartfabrika VSEGEI, St. Petersburg.
- Malitch, K.N., 2004. Morphology, chemistry, and Os isotope systematics of osmium minerals in the Guli pluton (Maimecha-Kotui province, Siberian craton), in: *Natural Resources of Taimyr [in Russian]*. Issue 2, pp. 258–276.
- Malitch, K.N., Lopatin, G.G., 1997a. Geology and origin of ultramafic rocks of the Guli pluton, in: *Mineral Resources of Taimyr [in Russian]*. Noril'sk–St. Petersburg, VSEGEI, Issue 2, pp. 86–103.
- Malitch, K.N., Lopatin, G.G., 1997b. Metallogeny of the Guli clinopyroxenite-dunite complex, northern Siberia, Russia: New data. *Geologiya Rudnykh Mestorozhdenii* 39 (3), 247–257.
- Malitch, K.N., Auge, T., Badanina, I.Yu., Goncharov, M.M., Junk, S.A., Pernicka, E., 2002. Os-rich nuggets from Au-PGE placers of the Maimecha-Kotui Province, Russia: a multi-disciplinary study. *Miner. Petrol.* 76, 121–148.
- Mallmann, G., O'Neill, H.St.C., 2009. The crystal/melt partitioning of V during mantle melting as a function of oxygen fugacity compared with some other elements (Al, P, Ca, Sc, Ti, Cr, Fe, Ga, Y, Zr and Nb). *J. Petrol.* 50 (9), 1765–1794.
- Manglik, A., Christensen, U.R., 2006. Effect of lithospheric root on decompression melting in plume–lithosphere interaction models. *Geophys. J. Int.* 164, 259–270.
- Mathez, E.A., 1976. Sulfur solubility and magmatic sulfides in submarine basalt glass. *J. Geophys. Res.* 81, 4269–4276.
- Mathez, E.A., 1984. Influence of degassing on oxidation-states of basaltic magmas. *Nature* 310 (5976), 371–375.
- Maurel, C., Maurel, P., 1982. Etude expérimentale de l'équilibre Fe²⁺-Fe³⁺ dans les spinelles chromifères et les liquides silicates basiques coexistants à 1 atm. *C.R. Acad. Sci. Paris* 285, 209–215.
- McKenzie, D., Bickle, M.J., 1988. The volume and composition of melt generated by extension of the lithosphere. *J. Petrol.* 29, 625–679.
- Mungall, J.E., Hanley, J.J., Arndt, N.T., Debecdelievre, A., 2006. Evidence from meimechites and other low-degree mantle melts for redox controls on mantle-crust fractionation of platinum-group elements, in: *Proceedings of the National Academy of Sciences of the United States of America* 103 (34), 12,695–12,700.

- Nikogosian, I.K., Sobolev, A.V., 1997. Ion-microprobe analysis of melt inclusions in olivine: Experience in estimating the melt-olivine partition coefficients of elements. *Geokhimiya* 35 (2), 155–157.
- Niu, Y.L., 2004. Bulk-rock major and trace element compositions of abyssal peridotites: Implications for mantle melting, melt extraction and post-melting processes beneath mid-ocean ridges. *J. Petrol.* 45, 2423–2458.
- Perchuk, L.L., Safonov, O.G., Yapaskurt, V.O., Barton, J.M., 2000. Crystal-melt equilibria involving potassium-bearing clinopyroxene as indicator of mantle-derived ultrahigh-potassic liquids: an analytical review. *Lithos* 60, 89–111.
- Petrinin, A.G., Sobolev, S.V., 2006. What controls thickness of sediments and lithospheric deformation at a pull-apart basin? *Geology* 34 (5), 389–392.
- Petrinin, A.G., Sobolev, S.V., 2008. Three-dimensional numerical models of evolution of pull-apart basins. *Phys. Earth. Planet. Inter.* 171, 387–399.
- Polyakov, A.N., Cundall, P.A., Podladchikov, Y.Y., Lyakhovsky, V.A., 1993. An explicit inertial method for the simulation of the viscoelastic flow: an evaluation of elastic effects on diapiric flow in two- and three-layers models, in: Stone, D.B., Runcorn, S.K. (Eds.), *Flow and Creep in the Solar System: Observations, Modeling and Theory*. Kluwer Academic Publishers, pp. 175–195.
- Portnyagin, M., Almeev, R., Matveev, S., Holtz, F., 2008. Experimental evidence for rapid water exchange between melt inclusions in olivine and host magma. *Earth Planet. Sci. Lett.* 272 (3–4), 541–552.
- Prytulak, J., Elliott, T., 2007. TiO₂ enrichment in ocean island basalts. *Earth Planet. Sci. Lett.* 263 (3–4), 388–403.
- Rudnick, R.L., 2002. Composition of the continental crust. *Treatise on Geochemistry* 3, 1–64.
- Ryabchikov, I.D., 2003. Mechanisms and conditions of magma generation in mantle plumes. *Petrologiya* 11 (6), 548–555.
- Ryabchikov, I.D., Kogarko, L.N., Solovova, I.P., 2009. Physicochemical conditions of magma generation at the base of the Siberian plume, from data on micrometric melt inclusions in meimechites and alkali picrites of the Maimecha–Kotui province. *Petrologiya* 17 (3), 311–322.
- Rybacki, E., Dresen, G., 2000. Dislocation and diffusion creep of synthetic anorthite aggregates. *J. Geophys. Res.* 105, 26017–26036.
- Saal, A.E., Hauri, E.H., Langmuir, C.H., Perfit, M.R., 2002. Vapour undersaturation in primitive mid-ocean-ridge basalt and the volatile content of Earth's upper mantle. *Nature* 419, 451–455.
- Sack, R.O., Carmichael, I.S.E., Rivers, M., Ghiorso, M.S., 1980. Ferric-ferrous equilibria in natural silicate liquids at 1 bar. *Contrib. Mineral. Petrol.* 75 (4), 369–376.
- Safonov, O.G., Perchuk, L.L., Litvin, Yu.A., 2005. Equilibrium K-bearing clinopyroxene–melt as a model for barometry of mantle-derived mineral assemblages. *Russian Geology and Geophysics (Geologiya i Geofizika)* 46 (12), 1300–1316 (1318–1334).
- Sheinman, Yu.M., 1947. A new petrographic province in the northern Siberian craton. *Izv. AN SSSR, Ser. Geol.*, No. 3, 15–28.
- Sobolev, A.V., 1996. Melt inclusions in minerals as a source of principle petrological information. *Petrology* 4, 209–220.
- Sobolev, A.V., Danyushevsky, L.V., 1994. Petrology and geochemistry of boninites from the north termination of the Tonga Trench: constraints on the generation conditions of primary high-Ca boninite magmas. *J. Petrol.* 35, 1183–1213.
- Sobolev, A.V., Slutskii, A.B., 1984. Composition and crystallization conditions of the initial melt of the Siberian meimechites in relation to the general problem of ultrabasic magmas. *Geologiya i Geofizika (Soviet Geology and Geophysics)* 12, 97–110 (93–104).
- Sobolev, A.V., Kamenetsky, V.S., Kononkova, N.N., 1991. New data on petrology of Siberian meimechites. *Geokhimiya*, No. 8, 1084–1095.
- Sobolev, A.V., Hofmann, A.W., Nikogosian, I.K., 2000. Recycled oceanic crust observed in 'ghost plagioclase' within the source of Mauna Loa lavas. *Nature* 404, 986–990.
- Sobolev, A.V., Hofmann, A.W., Sobolev, S.V., Nikogosian, I.K., 2005a. An olivine-free mantle source of Hawaiian shield basalts. *Nature* 434 (7033), 590–597.
- Sobolev, A.V., Hofmann, A.W., Kuzmin, D.V., Yaxley, G.M., Anderson, A.T., Arndt, N.T., Chung, S.-L., Garcia, M.O., Gurenko, A.A., Danyushevsky, L.V., Elliott, T., Frey, F.A., Kamenetsky, V.S., Kerr, A.C., Krivolutskaya, N.A., Matvienkov, V.V., Nikogosian, I.K., Rocholl, A., Sigurdsson, I., Suschevskaya, N.M., Teklay, M., 2007. The amount of recycled crust in sources of mantle-derived melts. *Science* 316 (5823), 412–417.
- Sobolev, A.V., Hofmann, A.W., Brüggmann, G., Batanova, G., Kuzmin, D.V., 2008a. A quantitative link between recycling and osmium isotopes. *Science* 321 (5888), 536.
- Sobolev, A.V., Krivolutskaya, N.A., Kuzmin, D.V., 2009a. Petrology of the parental melts and mantle sources of Siberian trap magmatism. *Petrology* 17, 253–286.
- Sobolev, N.V., 1974. Deep-Seated Inclusions in Kimberlites and the Problem of the Composition of the Upper Mantle [in Russian]. Nauka, Novosibirsk.
- Sobolev, N.V., Logvinova, A.M., Zedgenizov, D.A., Pokhilenko, N.P., Kuzmin, D.V., Sobolev, A.V., 2008b. Olivine inclusions in Siberian diamonds: high-precision approach to minor elements. *Eur. J. Miner.* 20, 305–315.
- Sobolev, N.V., Logvinova, A.M., Zedgenizov, D.A., Pokhilenko, N.P., Malygina, E.V., Kuzmin, D.V., Sobolev, A.V., 2009b. Petrogenetic significance of minor elements in olivines from diamonds and peridotite xenoliths from kimberlites of Yakutia. *Lithos*, doi:10.1016/j.lithos.2009.06.038.
- Sobolev, S.V., Babeyko, A.Yu., 1994. Modeling of mineralogical composition, density and elastic wave velocities in the unhydrous rocks. *Surveys Geophys.* 15, 515–544.
- Sobolev, S.V., Babeyko, A.Y., 2005. What drives orogeny in the Andes? *Geology* 33 (8), 617–620.
- Sobolev, S.V., Petrunin, A., Garfunkel, Z., Babeyko, A.Y., and DESERT Group, 2005b. Thermo-mechanical model of the Dead Sea transform. *Earth Planet. Sci. Lett.* 238, 78–95.
- Sobolev, V.S., 1936. Petrology of Siberian traps. *Transactions, All-Union Arctic Institute*, vol. XLIII, L., Izd. GU Sevmorputi.
- Sobolev, V.S., 1976. Generation of magmas and origin of igneous rocks, in: *Problems of Crustal and Upper Mantle Petrology [in Russian]*. IGIG SO RAN SSSR, Novosibirsk.
- Sobolev, V.S., Sobolev, A.V., 1977a. Eclogite barrier at recrystallization of native basaltoids under conditions of high pressures. *Dokl. Akad. Nauk* 237, 437–440.
- Sobolev, V. S., Sobolev, N. V., 1975. Problems of 2-Stage formation of Earth crust. *Dokl. Akad. Nauk SSSR* 221, 435–438.
- Sobolev, V.S., Sobolev, N.V., 1980. New evidence of the sinking to great depths of the eclogitized rocks of Earth crust. *Dokl. Akad. Nauk SSSR* 250, 683–685.
- Sobolev, V.S., Sobolev, S.V., 1977b. Mantle density changes associated with basaltic magma melting. *Dokl. Akad. Nauk SSSR* 234 (4), 896–899.
- Sobolev, V.S., Panina, L.I., Chepurov, A.I., 1972. Crystallization temperatures of minerals in meimechites, from homogenization of melt inclusions. *Dokl. Akad. Nauk SSSR* 205 (1), 201–205.
- Spandler, C., O'Neill, H.S.C., Kamenetsky, V.S., 2007. Survival times of anomalous melt inclusions from element diffusion in olivine and chromite. *Nature* 447 (7142), 303–306.
- Stoll, B., Jochum, K.P., Herwig, K., Amini, M., Flanz, M., Kreuzburg, B., Kuzmin, D., Willbold, M., Enzweiler, J., 2008. An automated iridium-strip heater for LA-ICP-MS bulk analysis of geological samples. *Geostand. Geoanal. Res.* 32 (1), 5–26.
- Tuff, J., Takahashi, E., Gibson, S.A., 2005. Experimental constraints on the role of garnet pyroxenite in the genesis of high-Fe mantle plume derived melts. *J. Petrol.* 46, 2023–2058.
- Vasiliev, Yu.R., 1978. Olivines in ultramafic rocks of the northern Siberian craton, in: *Petrology and Mineralogy of Ultramafic Rocks [in Russian]*. Nauka, Novosibirsk.
- Vasiliev, Yu.R., Zolotukhin, V.V., 1975. Petrology of Ultramafic Rocks in the Northern Siberian Craton and Some Problems of their Petrogenesis [in Russian]. Nauka, Novosibirsk.
- Vasiliev, Y.R., Zolotukhin, V.V., 1995. The Maimecha–Kotui alkaline-ultramafic province of the northern Siberian Platform, Russia. *Episodes* 18, 155–164.
- Walter, M.J., Bulanova, G.P., Armstrong, L.S., Keshav, S., Blundy, J.D., Gudfinnsson, G., Lord, O.T., Lennie, A.R., Clark, S.M., Smith, C.B.,

- Gobbo, L., 2008. Primary carbonatite melt from deeply subducted oceanic crust. *Nature* 454, 622–625.
- White, R.S., McKenzie, D., 1995. Mantle plumes and flood basalts. *J. Geophys. Res.* 100 (B9), 17,543–17,585.
- Wooden, J.L., Czamanske, G.K., Fedorenko, V.A., Arndt, N.T., Chauvel, C., Bouse, R.M., King, B.S.W., Knight, R.J., Siems, D.F., 1993. Isotopic and trace-element constraints on mantle and crustal contributions to Siberian continental flood basalts, Norilsk area, Siberia. *Geochim. Cosmochim. Acta* 57, 3677–3704.
- Yaxley, G.M., Brey, G.P., 2004. Phase relations of carbonate-bearing eclogite assemblages from 2.5 to 5.5 GPa: implications for petrogenesis of carbonatites. *Contrib. Mineral. Petrol.* 146, 606–619.
- Zhabin, A.G., 1965. Structure and formation succession of the Guli complex of dunite, ultramafic and ultramafic-alkali lavas, alkaline rocks, and carbonatites, in: Borodin, L.S. (Ed.), *Petrology and Chemistry of Ultramafic and Alkaline Rocks and Carbonatites* [in Russian]. Nauka, Moscow, pp. 159–192.